Doctoral Dissertation
Doctoral Program in Telecommunication Engineering (30th Cycle)

RF characterization and applications of carbon based composites

by

Ahmad Bayat

* * * * * *

Supervisor
Prof. Patrizia Savi

Doctoral Examination Committee:
Prof. Maurizio Bozzi, Referee, University of Pavia
Prof. Guido Gentili , Referee, Politecnic of Milan
Prof. Thomas Eibert,TUM, Germany
Prof. Alberto Tagliaferro, DISAT, Politecnico di Porino
Prof. Jean-Marc Tulliani, DISAT, Politecnico di Torino

Politecnico di Torino
October, 2018

I hereby declare that, the contents and organisation of this dissertation constitute my own original work and does not compromise in any way the rights of third parties, including those relating to the security of personal data.

…………………………………......
Ahmad Bayat
Turin, October 08, 2018

Summary

Graphene is a monolayer of carbon atoms with remarkable electronic and mechanical properties. The attractive electronic properties of thin and thick films made of carbon nanotubes (CNTs) and graphene are increasingly being exploited for environmental and biological sensors. In particular, their sensitivity, selectivity, fast response time, ability to operate at room temperature, and their passive nature (no power consumption) provide competitive advantages of CNTs in sensor applications. However, their design as RF wireless sensors requires the integration of an antenna with the sensor element. Moreover, while the plasmonic nature of graphene at terahertz frequency has been widely reported, investigations on the practical utility of graphene at the microwave frequencies used in wireless sensor nodes are sparse which is indicated in this thesis.

First, an ink comprising graphene thick films of different concentrations (12.5%, 25% and 33% in weight) is prepared for deposition, by screen printing. Detailed investigation of the surface morphology of the films using Scanning Electron Microscopy (SEM) and Atomic Force Microscopy (AFM) reveals that the graphene films present a homogeneous dispersion of the filler with a comparatively lower surface roughness at higher concentrations, and negligible agglomerates. The films are then printed in between copper electrodes on FR-4 substrate, commonly used in RF circuits, and the measured scattering parameters analyzed. A measurement-based RF equivalent circuit model of the graphene film is developed using a microstrip transmission line with a gap loaded by the film.

Second, investigation on various patch antennas with different substrates using Multi-Walled Carbon Nanotube (MWCNT) thin film deposition is addressed. Screen printing technique is used to insert a CNT film in a loading stub connected to the antenna patch. The variation of the CNT surface impedance modifies the resonant frequency from the reference value, as revealed by comparison of return loss measured with and without the CNT loading. This CNT stub loaded patch antenna can be used as a bio sensor.

Third, a printed RF slot ring resonator is configured with a graphene thin-film for sensor application. The conductive losses in the graphene film are characterized by dielectric spectroscopy and considered in the design. The graphene sensing element comprising the slot ring can be integrated with control electronics as a passive wireless sensor node. The novelty of this research is that RF losses are minimized by capacitively loading the ring at selective locations along its periphery. Dielectric spectroscopy is used to study variation in surface impedance of the film for various graphene loadings, and RF simulations are corroborated with measurements on graphene loaded slot ring resonators used in ammonia gas sensor application. The measurement steps are taken into consideration. As mentioned, the ring resonant frequency shift in presence of the ammonia gas is the factor used to sense the gas.

Fourth, a novel design of an aperture coupled antenna which is weakly coupled to an interdigitated capacitor (IDC) is presented that serves the dual purpose of antenna impedance matching and the sensing function, the latter enabled by a thick film of CNTs deposited on the IDC surface. Simulations using CNT films of varying conductivity (or surface impedance) reveal that a strong antenna resonance can be produced. Furthermore, a study of the patch antenna radiation pattern with and without the CNT film shows weak coupling between the film and the antenna (loss of 0.5 dB or less relative to patch alone). Thus, the sensor film and geometry can be independently optimized without affecting radiation pattern.

Keywords: *graphene, carbon nanotubes (CNTs), patch antenna, surface morphology, radio frequency (RF), microwave, resonator, screen printing, sensor, thin and thick films.*

Acknowledgment

This work was impossible without the cooperation of many people. First, I would like to acknowledge my advisor, Professor Patrizia Savi for her support, guidance and encouragement during this work. She has taught me many things about microwaves, research, experiments, simulations, presentation and being professional. Her high standards have been a blessing, and I have greatly appreciated her hospitality.

I would also like to especially acknowledge Dr. Simone Quaranta for his great support throughout the project. I must acknowledge Dr. Krishna Naishadham from Georgia Technology Institute and Dr. Langis Roy and Ololade Sanusi from UOIT of Canada for their great collaboration. Also, I should acknowledge Dr. Mario Miscuglio from Italian Institute of Technology (IIT) in Genova. I would like to thank Professors Ladislau Matekovits and Francesca Vipiana for their useful courses about nanomaterials and advanced antennas design. I would really appreciate Professor Alberto Tagliaferro and Dr. Mauro Giorcelli from Department of Applied Science and Technology (DISAT) for their collaboration in realizing the carbon-based composites. Gianluca Dassano is the other person I would like to acknowledge for his support in antenna laboratory in Politecnic of Turin. I would also thank my wife, Leila, for her patience and support during this period. Finally, I would like to express my sincere appreciation to the referee committee.

Most of all, I would like to thank God for everything.

Ahmad Bayat

October. 2018

I would like to dedicate
this thesis to my loving
wife and my little son.

Contents

1.Introduction 1
2. Carbon nanotubes and Graphene 3
  2.1. Carbon nanotubes 3
  2.2. Graphene 4
3. Morphological and RF Characterization of Graphene composite films 8
  3.1. Introduction 8
  3.1 Film Preparation 9
  3.2 Morphology Characterization 10
  3. 3. Electrical Characterization of Graphene Films 12
    3.3.1 Graphene Sheet Resistance 12
    3.3.2 Equivalent Microwave Circuit 13
4. CNT and Graphene stub-loaded patch antenna 19
  4.1 Patch Design 19
    4.1.1 Feed points 21
    4.1.2 Inset feed method 21
  4.2 First prototype antenna 22
    4.2.1 Simulation and Measurement 25
    4.2.2 Radiation pattern and Gain 27
    4.2.3 Parametric simulation 30
  4.3 Second prototype antenna 34
    4.3.1 Patch antenna with FR4 substrate 34
    4.3.2 Parametric analysis 35
  4.4 Patch antenna with Arlon substrate 37
5. Aperture Coupled Patch antenna 40
  5.1 Aperture Coupled Patch antenna Design 40
  5.2 ACP CNT loaded antenna Design 44
  5.3 ACP configuration with InterDigitated Capacitor (IDC) 46
  5.4 Simulation Results 48
6. Microwave Ring Resonator 51
  6.1 A copper-clad slotted Ring Resonator Design 51

6.2 Graphene loaded slotted Ring Resonator Design 51
6.3 Simulation and measurements 52
6.4 Equivalent Circuit Model of graphene film 54
6.5 Application as a gas sensor 56

Conclusion 59

List of Tables

Table 1. Sheet resistance of graphene films (Ωs per square). 13
Table 2. Surface impedance effect in ACP 46
Table 3. Surface impedance effect in ACP with IDC 49

List of Figures

Figure 1. Carbon nanotube types; (a) Single walled CNTs, (b) Multiwalled CNTs........................ 3
Figure 2. Carbon nanotubes application. 4
Figure 3. Graphene sheet and its carbon structure.. 5
Figure 4. Graphene Fermi surface and level.. 5
Figure 5. Inkjet printed Single walled CNT flexible TFT. 6
Figure 6. Graphene inks used for printed electronics. 7
Figure 7. Graphene application as gas sensors and bio sensors...................................... 7
Figure 8. Screen printing table.. 9
Figure 9. Steps of composite preparation. 10
Figure 10. Optical images (20X). Graphene 25% in weight (left image) and Graphene 33% in weight (right image).. 10
Figure 11. SEM images of Graphene 25% and 33% in weight. 11
Figure 12. AFM analysis of graphene films of 25% and 33% in weight. a) roughness; b) maximum cluster height; c) grain dimension.. 12
Figure 13. Four probe method: Solartron SI 1260 (left), sample holder (center), sample on FR4 2×1 cm (right). 13
Figure 14. Microstrip line with graphene thin film deposition in the gap. 14
Figure 15. Measured scattering parameters for a film with ethyl cellulose only and a film with graphene 12.5% in weight.. 14
Figure 16. Equivalent circuit model of Microstrip line with gap loaded by a graphene thick film. 15
Figure 17. Measurements (dashed line) and simulations (solid line) for the graphene film 12.5% in weight.. 16
Figure 18. Measurements (dashed line) and simulations (solid line) for the graphene film 25% in weight... 16
Figure 19. Transmission coefficient measurements.. 17
Figure 20. Measurements and simulations agreement of the transmission and reflection coefficients... 18
Figure 21. Microstrip patch antenna 19
Figure 22. Electric field lines.. 20
Figure 23. Side view of patch antenna.. 20
Figure 24. Inset feed microstrip patch antenna 22
Figure 25. CNT stub loaded patch antenna scheme... 23
Figure 26. Fabricated CNT loaded patch antenna 24

Figure 27. CNT loaded patch antenna schematic in HFSS 24
Figure 28. S11 measured and simulated results for reference and 3 layer CNT loaded antenna . 25
Figure 29. Measured and simulated S11 results for patch only and various CNT compositions . 26
Figure 30. Measured and simulated S11 results for patch only and various graphene compositions. 26
Figure 31. Parametric analysis on the film dimension 27
Figure 32. Measured and simulated radiation pattern (co-pol) of the reference uncoated antenna in the principal planes. 28
Figure 33. Measured and simulated radiation pattern (co-pol) of the CNT-loaded 3-layer antenna. 28
Figure 34. Normalized gain of patch+stub at 4.36 GHz. 29
Figure 35. Gain of patch+stub at 4.36 GHz 29
Figure 36. Normalized gain for CNT stub loaded antenna at 4.13 GHz 30
Figure 37. Gain of CNT stub loaded antenna at 4.13 GHz. 30
Figure 38. CNT loaded patch antenna- new design 31
Figure 39. Parametric simulation of surface impedance sheet reactance 31
Figure 40. Gain at R=50 Ω &Xs=-400. 32
Figure 41. Gain at R=50 Ω & Xs=-1200. 33
Figure 42. Gain at R=50 Ω & Xs=-2000. 33
Figure 43. CNT loaded patch design at 2.4 GHz 34
Figure 44. Parametric analysis of gap position with FR4 substrate 35
Figure 45. Stub width variation effects on results 36
Figure 46. CNT film dimension effects on the results 36
Figure 47. Normalized gain of CNT loaded patch antenna resonating at 2.4 GHz 37
Figure 48. CNT loaded patch antenna with Arlon substrate 38
Figure 49. Simulation results of the antenna with Arlon substrate 38
Figure 50. Normalized gain of CNT loaded patch antenna with Arlon substrate resonating at 2.4 GHz 39
Figure 51. Layers of Aperture Coupled Patch antenna 41
Figure 52. Feed line dimensions in aperture coupled antenna 41
Figure 53. Patch layer geometry 42
Figure 54. Feed layer geometry 42
Figure 55. Feed substrate and slot dimensions 43
Figure 56. Aperture coupled patch antenna HFSS model 43
Figure 57. Return loss of the aperture coupled patch antenna 44
Figure 58. CNT loaded ACP in HFSS. 45
Figure 59. Return loss simulation for various resistance and reactance of the surface impedance 45
Figure 60. Patch layer geometry 47
Figure 61. Feed layer geometry 47

Figure 62. (a) Proximity-coupled feed line with IDC connected in series. (b) The simulated 10 fingers IDC in HFSS. 48
Figure 63. HFSS model of ACP antenna with IDC 48
Figure 64. Return loss of the ADP_IDC patch sensor as a function of the film impedance. 49
Figure 65. Gain for the loaded ACP IDC with CNT film. 50
Figure 66. The slotted ring resonator and its realization with graphene thin film deposition. 52
Figure 67. Graphene loaded and unloaded ring resonator models in HFSS. 52
Figure 68. Tangential E field in base line ring resonator at 2.47 GHz. 53
Figure 69. Base line and Graphene loaded ring simulations and measurements. 54
Figure 70. Parametric simulation: X=0 & R=a varies from 1 to 61 Ω. 56
Figure 71. Photo of lab 57
Figure 72. Ampoule 57
Figure 73. The replaced plastic box 58
Figure 74. Measurement of graphene-loaded ring resonator in various ambient 58

Chapter 1

1.Introduction

Graphene is a monolayer of carbon atoms which exhibits remarkable electronic and mechanical properties. Graphene based nano-materials have gained a lot of interest for many applications. In this thesis, a graphene ink with two concentrations (25% in weight and 33% in weight) was prepared and deposited, by screen printing. A detailed investigation of the surface morphology of the films using Scanning Electron Microscope (SEM) and Atomic Force Microscopy (AFM) reveals that the graphene films present a homogeneous dispersion of the filler with a comparatively lower surface roughness at higher concentrations, and negligible agglomerates. The films were then printed between copper electrodes on FR-4 substrate, commonly used in RF circuits, and the measured scattering parameters analysed. Finally, the reflection coefficient of a patch antenna, fabricated on FR-4 substrate with and without a stub loaded by a thin film were measured.

Graphene is a monolayer of carbon atoms with remarkable electronic and mechanical properties amenable to several applications [41,48]. With proper solvent, surfactant and stabilizer chemistry, graphene flakes can be dispersed in different binders to produce inks with widely tunable rheology, which can be used with various printing methods to produce sensors [4-5]. Films can be realized with several techniques such as mechanical exfoliation of solvent assisted graphite and subsequent deposition by spin coating or drop casting [34], epitaxial growth [1,11], chemical vapour deposition [35], and more recently screen printing techniques [7,8].

Graphene films have found many applications due to their unique electronic properties. In particular, great attention has been devoted to the use of graphene for biosensors (see e.g., [4,36-37]), gas sensors (see e.g. [21,22]), metrological applications [16], and humidity and temperature monitoring [13], pressure [38]. Graphene has been widely analyzed at terahertz frequency (see e.g. [52]). Recently, the practical utility of graphene at microwave frequency has been investigated [19] and some applications as tunable devices introduced [16,44]. However, the material properties of Nano-materials such as carbon nanotubes and graphene films for different concentration of the filler at microwave frequencies is still at an early stage.

In this thesis, the material effects of graphene films are investigated at microwave frequency. In particular, scanning Electron Microscopy (SEM), Atomic Force Microscopy (AFM), measurements and electrical characterization are used as a powerful set of tools to directly correlate the nature of the Nano fillers with the morphology of the nanocomposite films. The films with three different concentrations (12.5% in weight, 25% in weight and 33% in weight) are printed on the gap of a microstrip line and the results of a full-wave model compared with the measured scattering parameters.

Moreover, the effect of Carbon nanotubes (CNT) and graphene films are investigated on stub of various patch antennas by simulation as well as the measurement. The simulations were done by ANSYS HFSS. A good agreement is seen between the measurements and simulations. The main objective is measuring the resonance frequency of the stub loaded patch antenna before and after deposition of graphene or CNT onto the gap existed in the stub. To be noted that two prototypes of patch antenna are taken into consideration. First prototype resonates at around 5 GHz while the second resonates around 2.4 GHz which is applicable in wireless communications. In addition, graphene or CNT is deposited on different substrates in order to compare the results and examine the differences. In any cases the appropriate dimensions for the patch antenna were calculated based on [28]. Besides, the parametric simulation is used to verify the effects of the film dimensions and the gap position on the resonance frequency. Gain and radiation pattern are the other important factors which have been measured and simulated for the Graphene/CNT stub loaded patch antenna.

Successively, a copper-clad slotted ring resonator loaded with graphene film is investigated. The ring itself resonates at 2.47 GHz while the ring with graphene shifts this frequency which can be sensed and used as a sensor. The ring with and without graphene 33% in weight was simulated by ANSYS HFSS as well as CST Microwave Studio. As the graphene film is simulated by a surface impedance Z=R+jX in HFSS, parametric simulation is used to examine the effects of R and X independently to show their influence on the resonance frequency as well as the return loss magnitude. Moreover, the circuit calculated for the gap with graphene is a parallel RC.

An Aperture Coupled Patch (ACP) antenna loaded with CNT film is the last antenna type which is considered. The aperture coupled antenna is designed to resonate at 2.45 GHz. The CNT film is loaded on the feed line in two ways. First, directly it was inserted at the end of the feed line and second, it is loaded on an InterDigitated Capacitor (IDC) which is located at the end of the feed line. A suitable IDC with 10 fingers was designed for this IDC benefit is having a better impedance match between the feed line and the patch. Consequently, adding IDC to the feed line helps to sense the frequency shift better and more precisely. Gain was also simulated for this prototype.

Chapter 2

2. Carbon nanotubes and Graphene

2.1. Carbon nanotubes

Carbon nanotubes (CNTs) constitute a unique class of materials with a wide range of applications. The sp^2 chemical bonding of carbon atoms in CNTs provides exceptional electronic, thermal and mechanical properties [35]. With proper solvent, surfactant or stabilizer chemistry, CNTs can be dispersed in different binders to produce inks with widely tunable rheology that can be used with various printing methods.

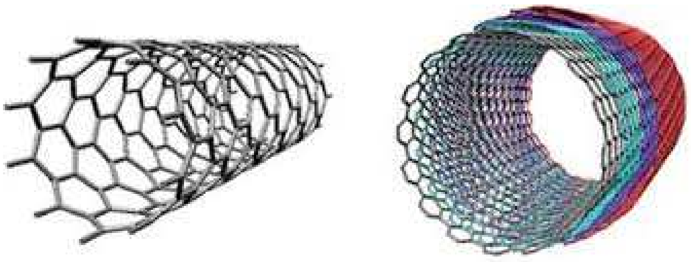

(a) (b)

Figure 1. Carbon nanotube types; (a) Single walled CNTs, (b) Multiwalled CNTs. (www.cheaptubes.com/product-category/single-walled-carbon-nanotubes/)

The robust stability of CNTs to mechanical, chemical, and thermal stress further improves device reliability in harsh environments and offers broad process compatibility for integration with dissimilar materials. In addition, with appropriate functionalization and dispersion, these materials are biocompatible, facilitating a range of applications in bio- integrated devices. The incorporation of CNTs in printed devices therefore offers numerous opportunities, both as an alternative to existing materials and in enabling novel applications as shown in Figure 2.

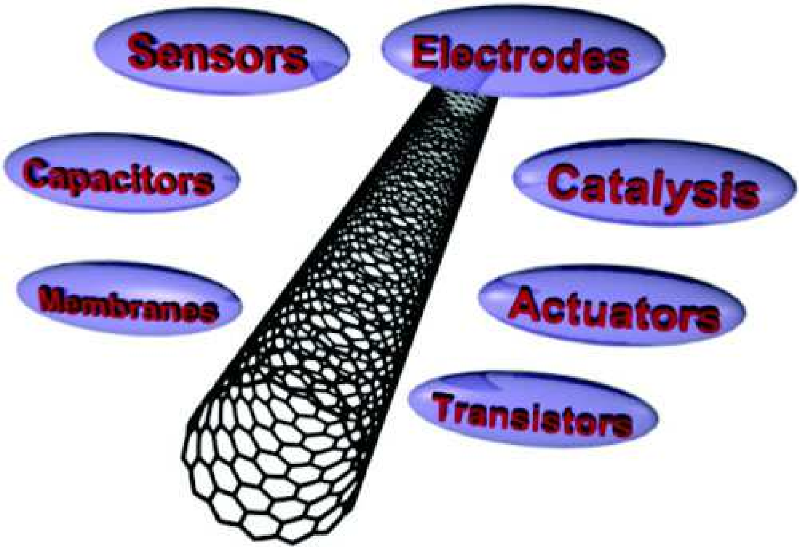

Figure 2. Carbon nanotubes application.
(www.cheaptubes.com/carbon-nanotubes-properties-and-applications/carbon-nanotubes-applications-2)

2.2. Graphene

Graphene films have found many applications due to the unique electronic properties of graphene [1]. Films can be realized with several techniques such as mechanical exfoliation of solvent assisted graphite and subsequent deposition by spin coating or drop casting, epitaxial growth, chemical vapor deposition, and more recently screen printing techniques [6,9].

Graphene is a 2D structure with sp^2 chemical bonding of carbon atoms, shown in Figure 3, providing remarkable electronic and mechanical properties [35]. Graphene based nano-materials have gained a lot of interest for developing sensors of various types [3-5]. With proper solvent, surfactant or stabilizer chemistry, graphene flakes can be dispersed in different binders to produce inks with widely tunable rheology, which can be used with various printing methods to produce sensors [5].

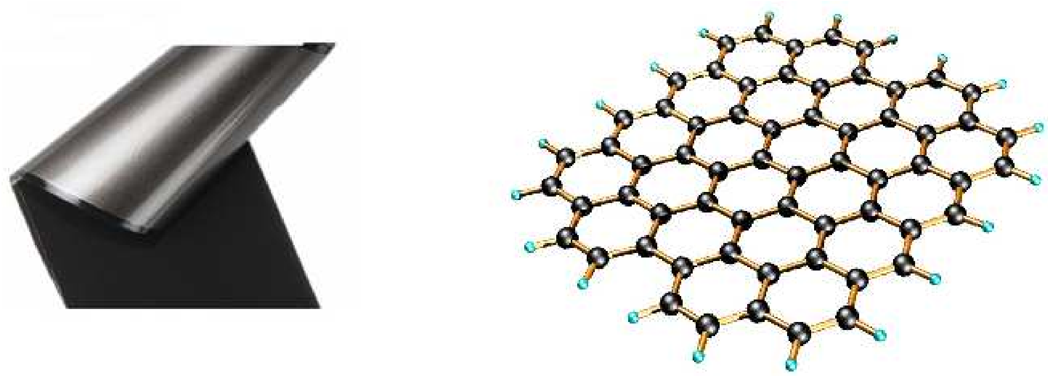

Figure 3. Graphene sheet and its carbon structure.
(www.azom.com/article.aspx?ArticleID=14826)

Graphene has different electronic structure respect to normal 3D materials. The Fermi surface including six double cones when the connection points of the cones (Dirac pointe) make its Fermi level as shown in Figure 4. An electric field can change the Fermi level in order to have either n-doped or p-doped materials. To be noted that the conductivity of doped graphene can even be higher than of copper. It is so transparent which in optical region just absorbs 2.3% of the light. It is worth mentioning some of its common properties with carbon nanotubes; Being stronger than steel, very stretchable and the possibility to be used as flexible conductor. Moreover, graphene thermal conductivity is so higher than the silver.

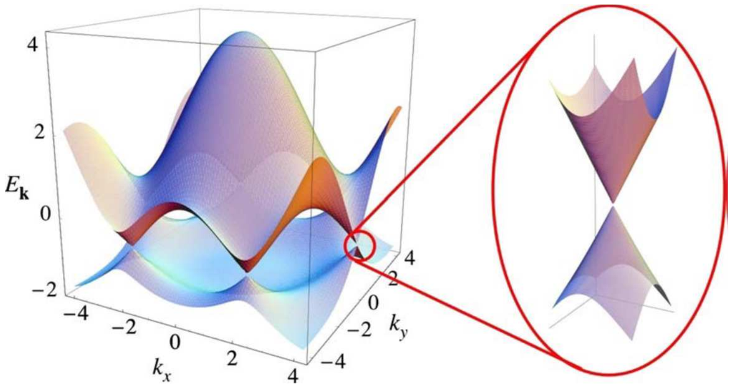

Figure 4. Graphene Fermi surface and level.
(www.mdpi.com/2076-3417/4/2/305/htm)

In particular, great attention has been devoted to the use of graphene for gas sensors (see e.g [8-9]), biosensors (see e.g., [4]), chemical sensors [11], metrological applications [13], and humidity and temperature monitoring [13].

In addition, the pervasive use of wireless technologies in the Internet of Things mobile devices for health applications, real-time sampling of the spatial and temporal distributions of environmental pollutants in cities, etc., increases the demand for miniaturized wireless sensor nodes for portable and wearable applications. Nanotechnology-based sensors capable of being integrated in wireless sensor nodes have been investigated in [15,44], primarily focusing on antenna design. However, the material properties of nano-materials such as carbon nanotubes and graphene films at microwave frequencies have not been addressed.

Recently, thin-films comprising single-walled carbon nanotubes (CNTs) [6] and multi-walled CNTs [7] have been shown to tune microstrip patch antennas by controlling the film deposition. Preliminary study indicated that the frequency shift produced by CNT loading of a patch antenna may be used as a discriminator for gas sensing [8]. The film’s reactance is changed by exposing it to the gas, resulting in shift of the resonant frequency. However, in prior investigations [8] the patch or any microstrip resonator needs to be in direct contact with the CNT thin film, which impacts the quality factor detrimentally. Therefore, nanomaterial-embedded microstrip resonators have limited utility in environmental sensing, wherein low concentrations of harmful gases such as ozone (60-80 parts per billion) need to be detected in ambient air. The high sensitivity required of these ambient sensors calls for improving the quality factor of the RF resonator, which is achieved by parasitically loading the resonator.

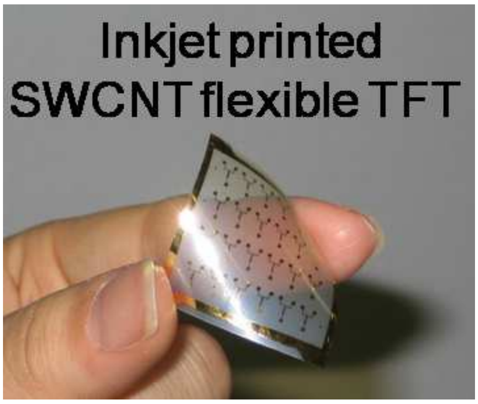

Figure 5. Inkjet printed Single walled CNT flexible TFT.
www.spie.org/newsroom/3169-cheap-green-printed-electronics?SSO=1

Moreover, with proper solvent, surfactant and stabilizer chemistry, graphene flakes can be dispersed in different binders to produce inks with widely tunable rheology, which can be used with various printing methods to produce sensors [2-4]. Films can be realized with several techniques such as mechanical exfoliation of solvent assisted graphite and subsequent deposition by spin coating or drop casting [34], epitaxial growth [1], chemical vapour deposition [35], and more recently screen printing techniques [9].

Figure 6. Graphene inks used for printed electronics.
www.graphene-info.com/taxonomy/term/63/all

Graphene has been widely analyzed at terahertz frequency. Recently, the practical utility of graphene at microwave frequency has been investigated [19,44] and some applications as tunable devices introduced [14,16,44]. However, the material properties of Nano-materials such as carbon nanotubes and graphene films for different concentrations of the filler at microwave frequencies is still at an early stage.

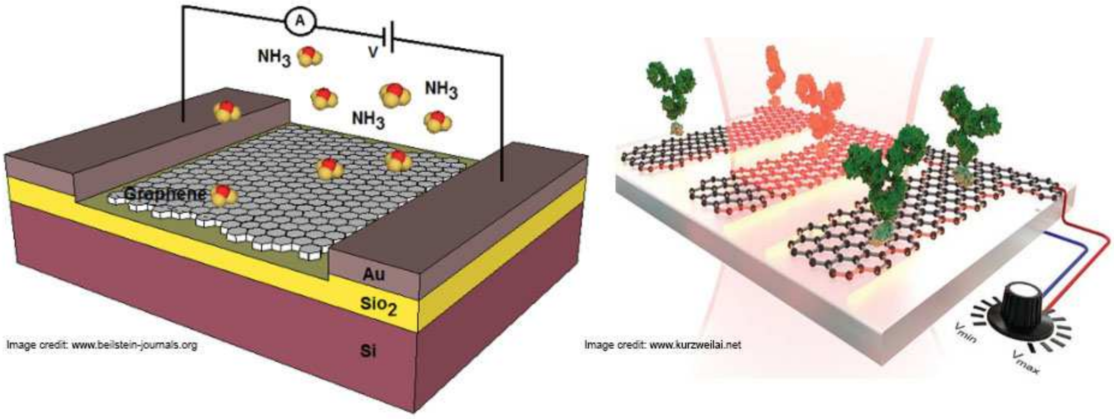

Image credit: www.beilstein-journals.org

Image credit: www.kurzweilai.net

Illustration of graphene based ammonia sensor

Illustration of graphene based bio-sensor

Figure 7. Graphene application as gas sensors and bio sensors.
https://www.beilstein-journals.org/bjnano/articles/5/85

Chapter 3

3. Morphological and RF Characterization of Graphene composite films

3.1. Introduction

Thanks to unique electronic properties of graphene, it is used in various applications. Several techniques are used for realization of graphene films such as mechanical exfoliation of solvent assisted graphite and subsequent deposition by spin coating or drop casting, epitaxial growth, chemical vapor deposition, and more recently screen printing techniques [30-33].

Various types of the sensors are realized and developed by utilizing graphene-based nano materials [41-45]. If solvent, surfactant and stabilizer chemistry are chosen properly, graphene flakes can be dispersed in different binders. As a consequent, inks with widely tunable rheology are produced in order to be used in various printing methods to realize different sensors [37]. The most important sensors which utilize the graphene films in their structure, are gas sensors (see e.g [21]), biosensors [36-37], chemical sensors [10], metrological applications [39-40] and humidity and temperature monitoring [13].

Using wireless technology abundantly in Internet of Things, mobile devices for health applications, real-time sampling of the spatial and temporal distributions of environmental pollutants in cities draws the market attention to miniaturized wireless sensor nodes for portable and wearable applications. Therefore, engineers try to design wireless sensors in such a way that nanotechnology-based sensors can be integrated in their structures [22], [44]. To be noted that the properties of nano materials such as carbon nanotubes and graphene films have not been investigated adequately.

In this chapter, microwave applications of the graphene films are under investigation. Screen printing technique prepares an ink comprising different concentrations of graphene thick films (12.5%, 25% or 33% in weight). Especially, SEM, AFM, Raman spectroscopy measurements and electrical characterization are used as a powerful set of tools to directly correlate the nature of the nanofillers with the morphology of the nanocomposite films and their bulk electrical and electromagnetic properties.

Moreover, two concentrations of graphene ink including 25% and 33% in weight are prepared and deposited by screen printing technology. The surface morphology is applied on the films by using the two methods of Scanning Electron Microscope (SEM) and Atomic Force Microscopy (AFM). The morphology reveals that the graphene films present a homogeneous dispersion of the filler with comparatively lower surface roughness at higher concentrations and negligible agglomerates. Then the produced graphene films are printed onto FR4 substrate between copper electrodes normally used in RF circuits in order to measure the scattering parameters.

3.1 Film Preparation

Screen-printing is used to deposit graphene as a thick film (each layer is about 10 µm thick) across the gap between two electrodes. The screen printing table is shown in Figure 8.

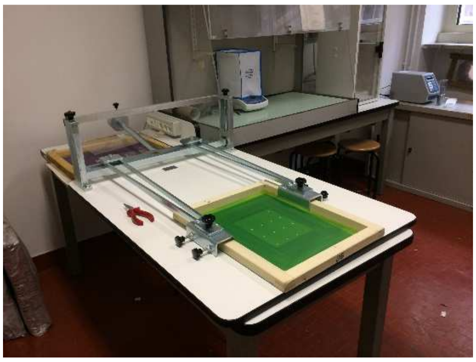

Figure 8. Screen printing table (Carbon group Laboratory, DISAT)

The relative composition of screen printing paste is defined by a procedure implied in [16]. Graphene 12.5% in weight is a combination of 9.4% in weight ethyl cellulose and 78.1% terpineol. 7.5% in weight of castor oil (Sigma Aldrich) is added to graphene films to ameliorate its dispersion and make 25% in weight graphene films. Ethyl cellulose plays 3 important roles as film binder, rheology modifier and steric stabilizer. The combination of α-Terpineol as a high boiling point solvent and Ethanol as a volatile solvent is sonicated by a titanium ultrasonic horn for 16 hours. The result is evaporation of the solvents and remaining a printable paste. The films size of 3×3 mm^2 is chosen to be printed across the gap between copper electrodes etched on the FR-4 substrate. Serigraphy is used to deposit the graphene films with thickness of 10-20 µm on thr FR4 substrate. Figure 9 shows the steps of composite preparation in brief.

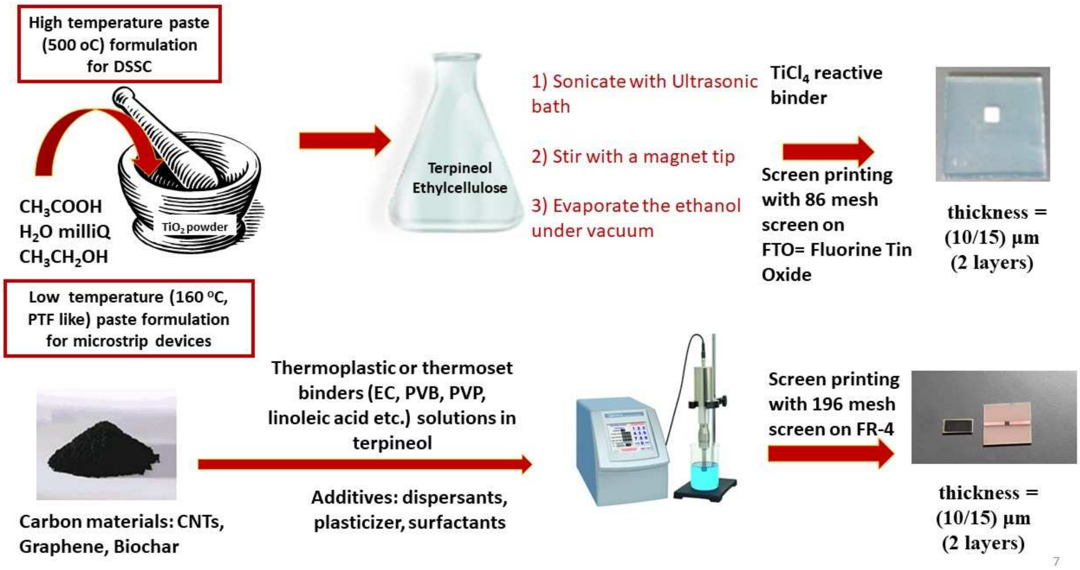

Figure 9. Steps of composite preparation.
https://ieeexplore.ieee.org/document/8477446

3.2 Morphology Characterization

A strong set of tools can be utilized to bind the morphology of the nanocomposite films with their bulk electrical and electromagnetic properties. Optical images, SEM, AFM and linked electrical characterization are accounted as these useful tools. Figure 10 shows the optical image of graphene 25% and graphene 33% in weight.

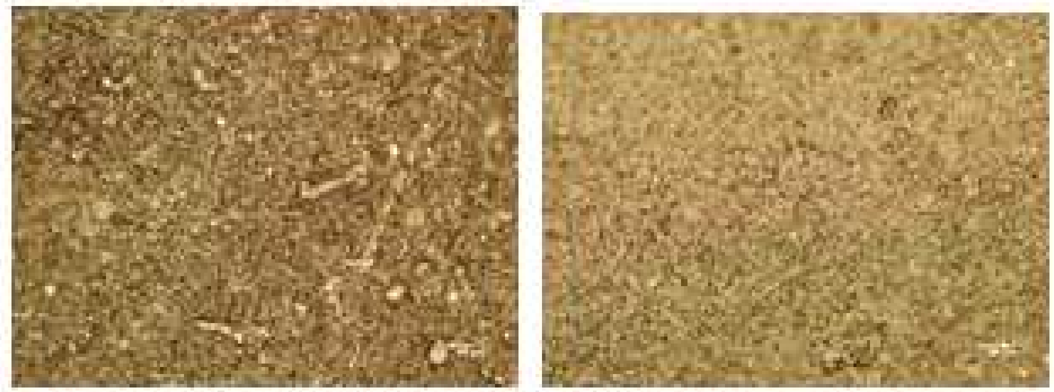

Figure 10. Optical images (20X). Graphene 25% in weight (left image) and Graphene 33% in weight (right image)
https://ieeexplore.ieee.org/document/8477446

The investigation on the surface topography was done by using a beam acceleration voltage of 5 kV via a Scanning Electron Microscope (SEM) measurement method. SEM analysis shows that graphene flakes of 25% and 33% in weight were uniformly dispersed throughout their films as shown in Figure 11.

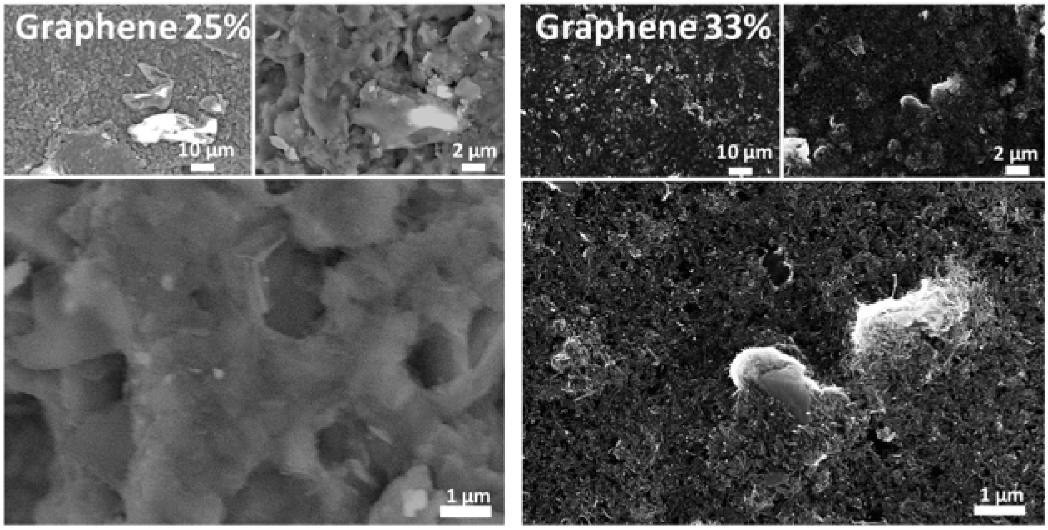

Figure 11. SEM images of Graphene 25% and 33% in weight.
www.mdpi.com/2311-5629/4/2/32/pdf

Moreover, Atomic force microscopy (AFM) measurement method is used to analyze the polymers including graphene flakes with the lateral sizes of few micrometers. It was done in room temperature by using SPI 4000 system in tapping mode. The polymers under measurement were shown different topological characteristics. The log-normal distribution is applied on the measured data in order to gain the clusters thickness and the grain distribution lateral size as well. The AFM images are seen in Figure 12. accompanied with the relevant analysis. The both SEM and AFM images and analysis demonstrate a homogenous dispersion of the filler and negligible agglomerates in graphene films under investigation.

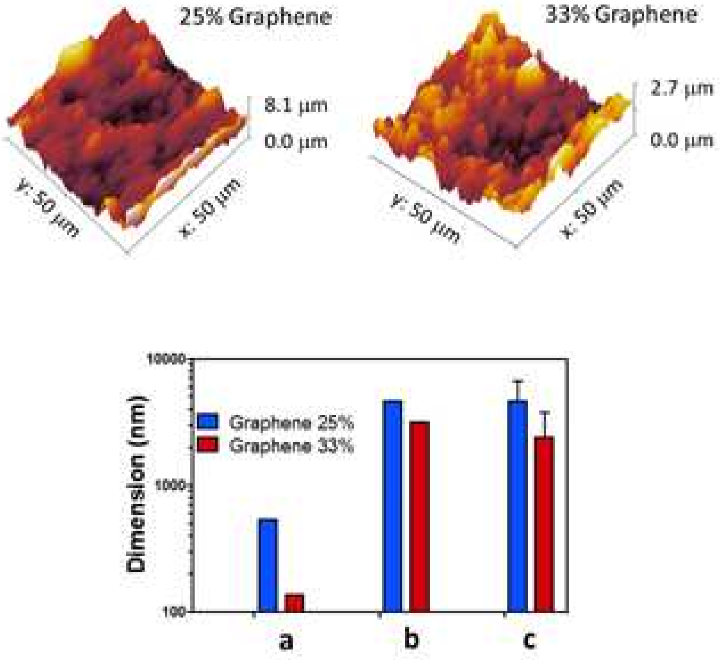

Figure 12. AFM analysis of graphene films of 25% and 33% in weight. a) roughness; b) maximum cluster height; c) grain dimension
www.mdpi.com/2311-5629/4/2/32/pdf

3. 3. Electrical Characterization of Graphene Films

3.3.1 Graphene Sheet Resistance

Resistance measurement has been done on one or two-layer graphene film. To be noted that each layer has almost 10 µm thickness and the graphene film was deposited on FR4 substrate by screen printing technique. The graphene sheet resistance is measured by using the four-probe method with a Solatron 1286 electrochemical interface as shown in Figure 13.

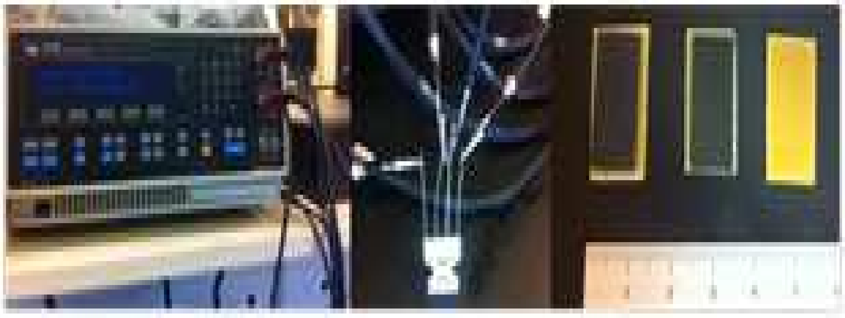

Figure 13. Four probe method: Solartron SI 1260 (left), sample holder (center), sample on FR4 2×1 cm (right).

The measurements have been tabulated in Table 1. As it is expected, the sheet resistance is inversely proportional to the thickness of the film; it means that increasing concentration of graphene flakes leads to decreasing the sheet resistance. As it is seen in the table 3.1, the graphene film with low concentration of 12.5% in weight is approximately as high as the resistance of the binder ethyl cellulose. It is crystal clear that the higher concentration graphene films, with 33% in weight, are of special interest to RF applications because of having higher conductivity and consequently lower resistance from 25 to 200 Ω.

Table 1. Sheet resistance of graphene films (Ωs per square).

Sample	One-layer	Two-layer
Ethyl cellulose	> 2e8	> 2e8
12.5 wt.%	2e7	2e6
25.0 wt.%	650	440
33.0 wt.%	240	160

3.3.2 Equivalent Microwave Circuit

The goal of this section is to investigate the behaviour of graphene films at microwave frequencies by depositing the films into the gap made in the middle of the transmission microstrip line as shown in Figure 14. Successively, its equivalent microwave circuit is designed and calculated for graphene film of 25% in weight.

Figure 14. Microstrip line with graphene thin film deposition in the gap.

The line width is 3 mm and the gap spacing is 2.6 mm. Photo etching is used to put the line on a FR4 substrate with thickness of 1.56 mm. To be noted that FR4 nominal relative permittivity is 4.3 when its loss tangent is 0.03. Regarding the deposition technique explained in previous section, a two-layer graphene film with dimensions of 3×3 mm^2 is screen printed on the mentioned gap. The measured scattering parameters for a film with ethyl cellulose only and a film with graphene 12.5% in weight are displayed in Figure 15.

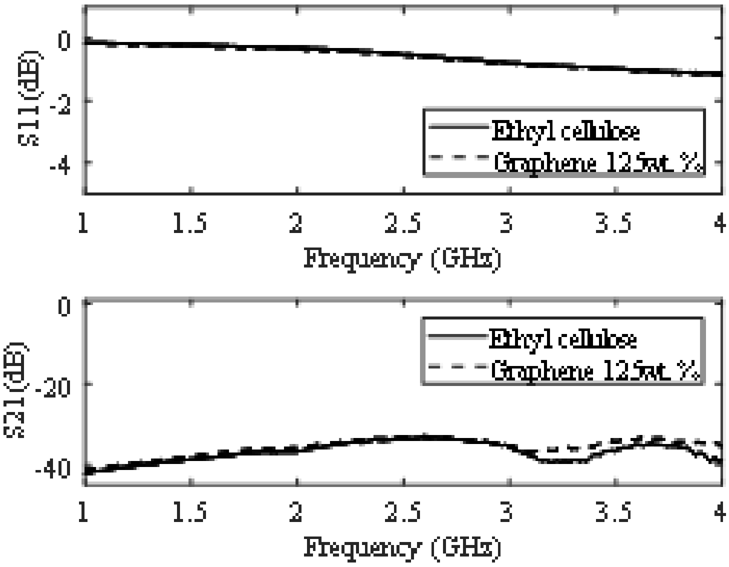

Figure 15. Measured scattering parameters for a film with ethyl cellulose only and a film with graphene 12.5% in weight.

It is seen that a film with graphene 12.5% in weight has the same transmission coefficients as a film only with binder. Next step is proceeding with measurements and simulations of the microstrip transmission line for various graphene loading arrangements. An unfilled gap has similar low transmission as the binder, thus confirming its insulating behavior.

In addition, A circuit model for the graphene thick film is derived using Advanced Design System (ADS) simulations by fitting the amplitude and phase of the measured S-parameters. the symmetrical circuit topology of this ADS model is shown in Figure 16. The resistance represents loss of the graphene film, and is the most important parameter in RF design. Since graphene is a conductive material (it has enhanced conductivity due to large surface area), the film across the gap can be represented by a resistance in parallel with a capacitance (which represents the gap capacitance). The capacitance in the series path has a very small value (less than 2 pF) and therefore it does not influence the equivalent circuit (hence not shown in Figure 16.).

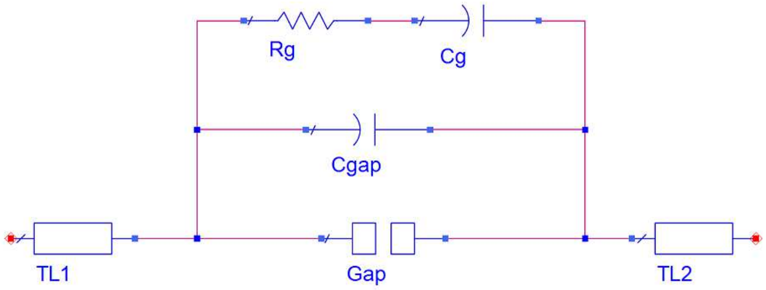

Figure 16. Equivalent circuit model of Microstrip line with gap loaded by a graphene thick film.

First, a line with a gap (no graphene film) is modeled using the microstrip gap, an additional capacitance (C_{gap} = 0.01 pF) and microstrip line models available in ADS library. The binder in the gap and the graphene film 12.5% in weight behave the same way as the microstrip line with an unloaded gap. The film composed of 25% in weight of graphene film can be represented with RC elements (R_g = 291 Ω, C_g = 0.8 pF) in parallel as shown in Figure 16.

Measurements and model-derived fitted data are compared in Figure 17 and Figure 18 for the case of graphene films 12.5% and 25% in weight, respectively. Good agreement is observed between the circuit model and the measurements over 1-5 GHz range.

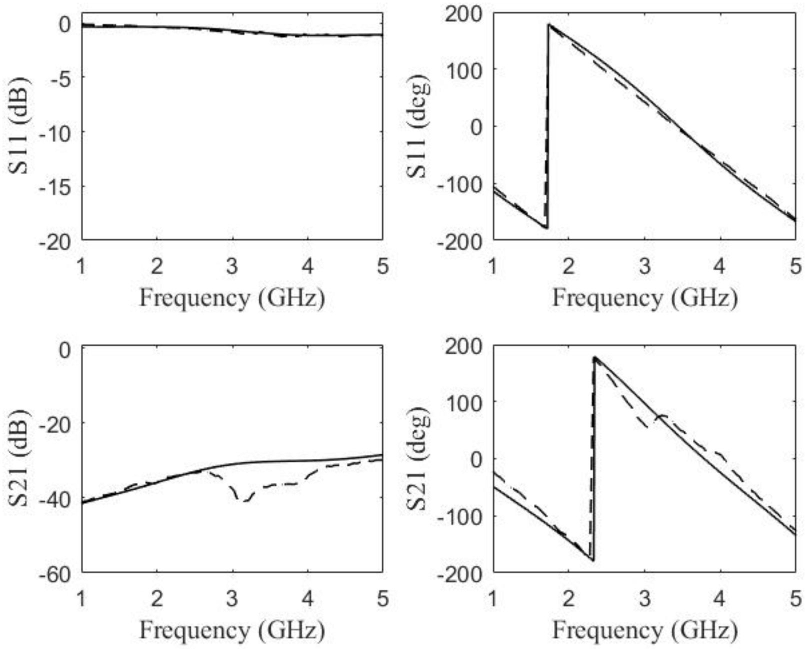

Figure 17. Measurements (dashed line) and simulations (solid line) for the graphene film 12.5% in weight.
www.jpier.org/PIERL/pierl76/06.18040903.pdf

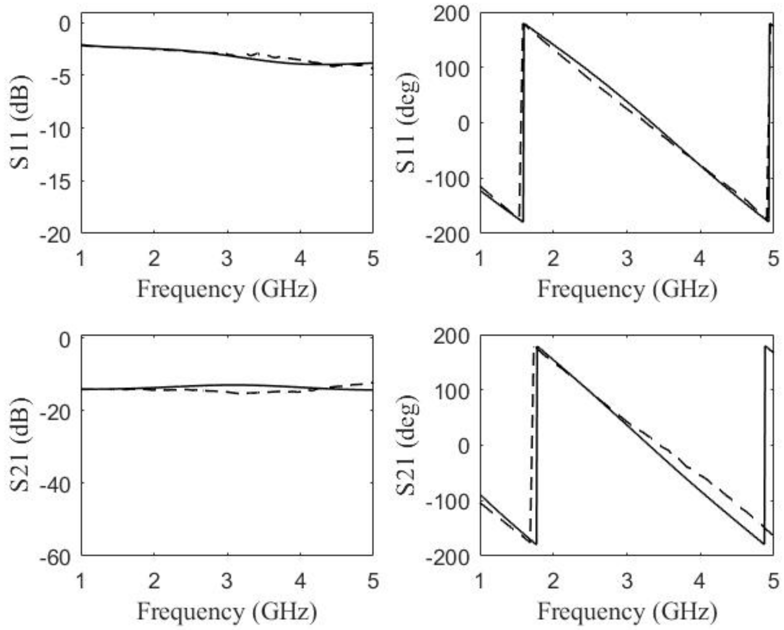

Figure 18. Measurements (dashed) and simulations (solid) for the graphene film 25% in weight.
www.jpier.org/PIERL/pierl76/06.18040903.pdf

Measurements of the transmission coefficient of the reference line as well as the microstrip line with gap for various graphene-loading compositions are shown in Figure 19.

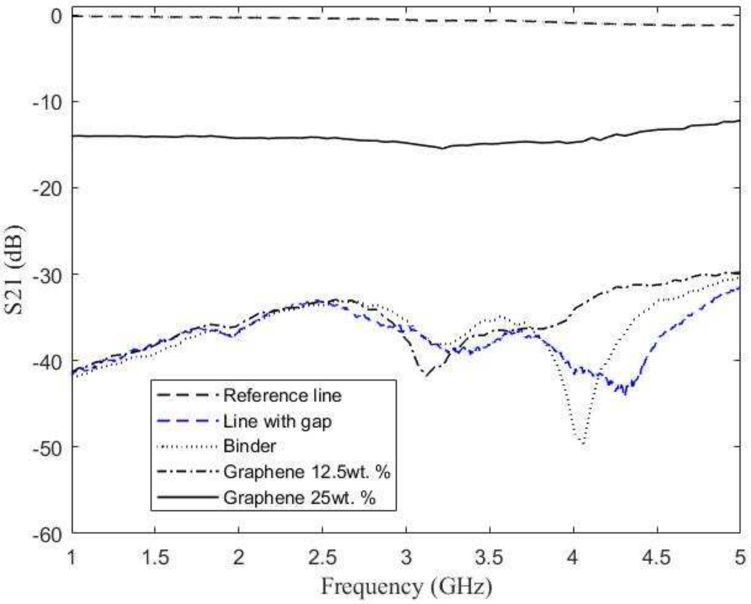

Figure 19. Transmission coefficient measurements.
www.jpier.org/PIERL/pierl76/06.18040903.pdf

On the other hand, the measured S-parameters for various graphene loading arrangements are shown in Figure 20. and compared with the results of a full-wave analysis obtained with HFSS. In the full-wave analysis, the film deposition is modeled as a surface impedance of values Z=(1e6-j150) ohms for the case of graphene film 12.5% in weight, Z=(450-j120) ohms for the case of graphene 25% in weight and Z=(160-j100) ohms for the case 33% in weight. The graphene film 33% in weight shows a marked increase in transmission across the gap due to reduced sheet resistance.

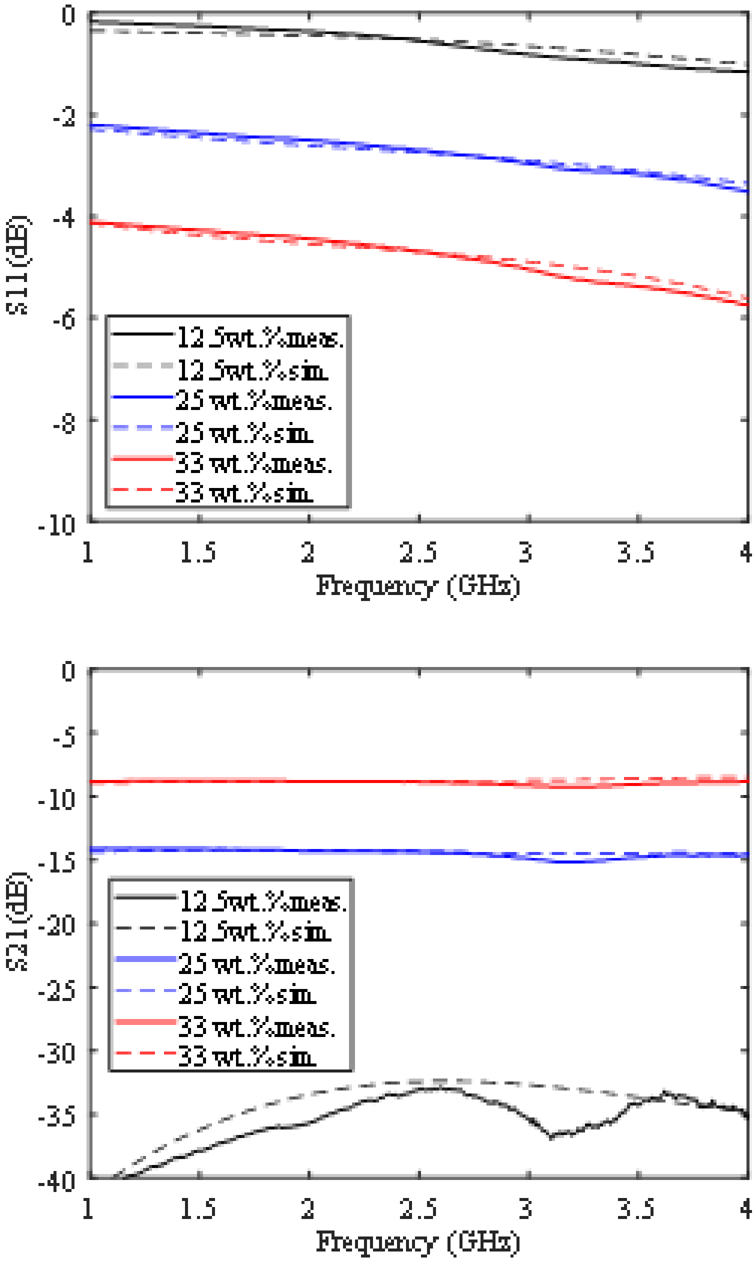

Figure 20. Measurements and simulations agreement of the transmission and reflection coefficients.
https://ieeexplore.ieee.org/document/8477446

Chapter 4

4. CNT and Graphene stub-loaded patch antenna

4.1 Patch Design

Microstrip patch antenna is so popular to be used in a range of frequency from 1 to 6 GHz. Since the communication systems were developed in 1970s, the need for the patch antennas with its proper dimension and performance were being emerged. The flat form and convenient weight in comparison with the parabolic reflectors and other huge antennas, pave the way for it to be a useful nominate in airborne and spacecraft applications. Currently, by taking advantage of high dielectric constant materials, its size reduced more which is suitable to use in handsets, GPS receivers and other mass-produced wireless devices [10]. Application of the patch antenna can be widely seen in 2.4 GHz or 5 GHz WLAN systems. Therefore, the next step is to proceed to design a patch antenna in order to meet the requirements. Figure 21 shows the configuration of the microstrip patch antenna.

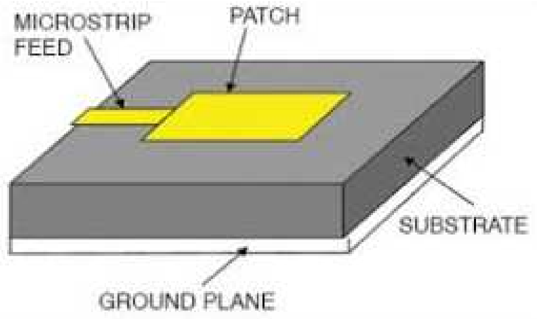

Figure 21. Microstrip patch antenna
https://ieeexplore.ieee.org/document/7523197

The fundamental design is starting with calculating the correct amplitudes for the length (L) and width (W) of the patch. As it is shown in Figure 22. parts of electric field lines on slots reside in air. As a consequent, the phase velocity varies in air and substrate causes that TEM mode is not supported by the transmission line. So, the quasi-TEM mode would be the dominant mode.

Accordingly, an effective dielectric constant (ε_{eff}) is considered to take it into account also the effect of fringing fields and the wave propagation in the line.

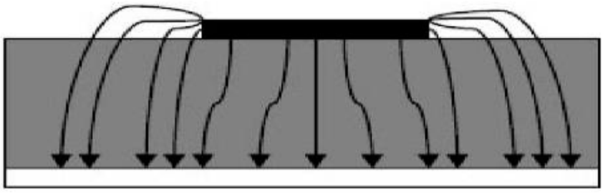

Figure 22. Electric field lines
www.ijser.org/paper/Design-And-Simulation-Of-Microstrip-Patch-Arrayantenna-For-Wireless-Communications-At-2.4-Ghz.html

Since some parts of fringing fields are in the air and not concentrated entirely in substrate as shown in Fig 4.2 , the ε_{eff} is less than ε_r.

$$\varepsilon_{\mathrm{eff}} = \frac{\varepsilon_r + 1}{2} + \frac{\varepsilon_r - 1}{2}\left[1 + 12\frac{h}{w}\right]^{-1/2} \tag{1}$$

where,

$\varepsilon_{\mathrm{eff}}$ = Effective dielectric constant
ε_r = Dielectric constant of substrate
h = Height of dielectric substrate
W = Width of the patch

TM_{10} dominant mode is propagating only if the patch length would be $\lambda_{eff}/2$ which is slightly less than λ/2. The TM_{10} mode indicates that the field varies one λ/2 cycle along the length while there is no variation along the width of the patch. Therefore, the voltage is maximum along the patch width while the current is minimum according to the open ends.

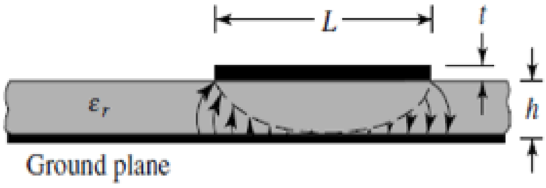

Figure 23. Side view of patch antenna
www.ijser.org/paper/Design-And-Simulation-Of-Microstrip-Patch-Arrayantenna-For-Wireless-Communications-At-2.4-Ghz.html

The normal elements are cancelling each other whereas the tangential ones are in phase and fortifying each other results in maximizing the radiated field. The edge connected to feed line as well as the opposite one are radiating edges which act as slot antennas whose gaps are via the patch edge and the ground plane. The fringing field yields that the electrical dimension of the patch looks bigger than the physical size with the extension of ΔL in each edge.

$$\Delta L = 0.412h\frac{(\varepsilon_{eff}+0.3)(\frac{w}{h}+0.264)}{(\varepsilon_{eff}-0.258)(\frac{w}{h}+0.8)} \tag{2}$$

Thus, the physical patch length L is:

$$L = L_{eff} - 2\Delta \mathrm{L} \tag{3}$$

In other words, the L_{eff} is calculated by a given resonance frequency f_r:

$$L_{eff} = \frac{C}{2f_r\sqrt{\varepsilon_{eff}}} \tag{4}$$

The resonance frequency f_r for any $\mathrm{TM_{mn}}$ mode in rectangular patch antenna is:

$$f_r = \frac{C}{2\sqrt{\varepsilon_{eff}}}[(\frac{m}{L})^2 + (\frac{n}{W})^2]^{1/2} \tag{5}$$

For having better radiation, the patch width is estimated as:

$$w = \frac{C}{2f_r\sqrt{\frac{\varepsilon_r+1}{2}}} \tag{6}$$

Feed line width formula is:

$$w_{feed} = \frac{7.48\times h}{e^{(Z_0\frac{\sqrt{\varepsilon_r+1.41}}{87})}} - 1.25\times t \tag{7}$$

4.1.1 Feed points

The variable factor in patch antenna is related to the feed method in order to provide the desired feed point impedance which matches the patch impedance and control the polarization. The three usual methods are Inset feed, coaxial feed and Aperture coupled patch antenna. In this thesis, the inset feed and aperture coupled ones are taken into consideration. It is noted that the aperture coupled patch antenna will be described in Chapter 5.

4.1.2 Inset feed method

The important factor in Inset feed is calculating *d* in order to match the patch with the input impedance of 50 Ωs:

$$d = \frac{L}{\pi}\cos^{-1}\left(\sqrt{\frac{Z_{in}}{R_{in}}}\right) \tag{8}$$

Z_{in} *and* R_{in} are referred to input resonance impedance and input resonance resistance.

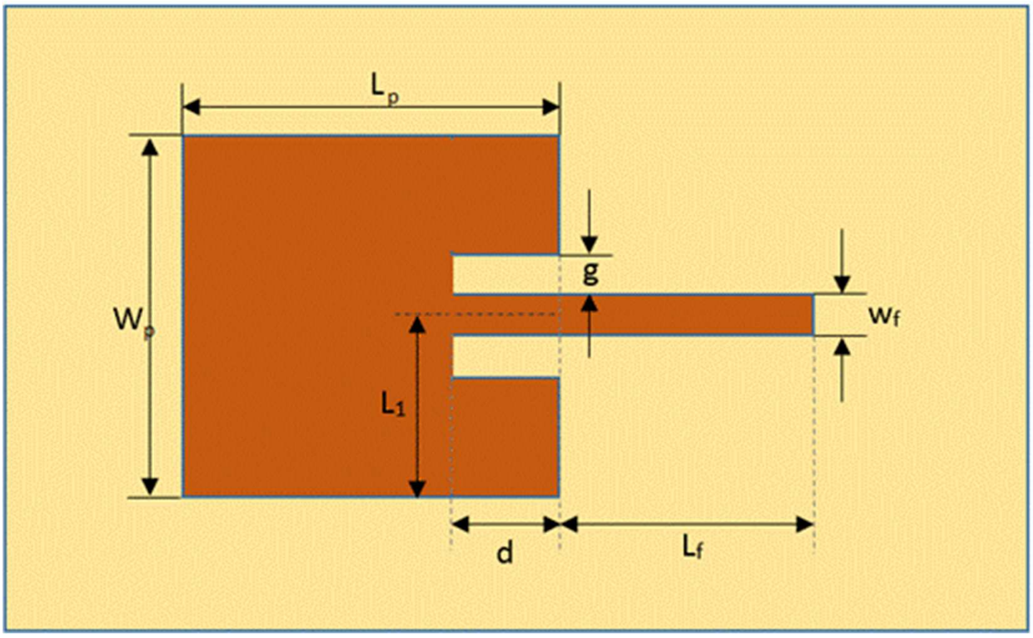

Figure 24. Inset feed microstrip patch antenna

4.2 First prototype antenna

First prototype antenna implies a design of an inset feed patch antenna with graphene or CNT stub loaded which the patch itself resonates around 5 GHz. To obtain this goal, first we start to design an inset feed patch antenna with FR4 substrate. The parameters and its calculation are as following:

FR4 substrate characteristics which used in this project are:

- Height (h) = 1.6 mm
- Permittivity (ε_r)= 4.35
- Loss tangent = 0.03
- Resonance frequency (f_r)= 4.9 GHz
- Patch width = 12 mm

$$\varepsilon_{\text{eff}} = \frac{4.35+1}{2} + \frac{4.35-1}{2}\left[1 + 12\frac{1.6}{12}\right]^{-1/2} = 3.7$$

$$\Delta L = 0.412(1.6)\frac{(3.7+0.3)(\frac{12}{1.6}+0.264)}{(3.7-0.258)(\frac{12}{1.6}+0.8)} = 0.72 \text{ mm}$$

$$L_{eff} = \frac{300}{2(4.9)\sqrt{3.7}} \approx 16 \text{ mm}$$

$$L = L_{eff} - 2\Delta\mathrm{L} = 16\text{-}2(0.72) \approx 15 \text{ mm}$$

$$w_{feed} = \frac{7.48\times1.6}{e^{\left(50\times\frac{\sqrt{4.35+1.41}}{87}\right)}} - 1.25\times0.035 \approx 3 \text{ mm}$$

Inset feed = 7 mm

The substrate and ground plane dimension are the same and set to 52×52 mm. The schematic figure of this design is shown in Figure 25.

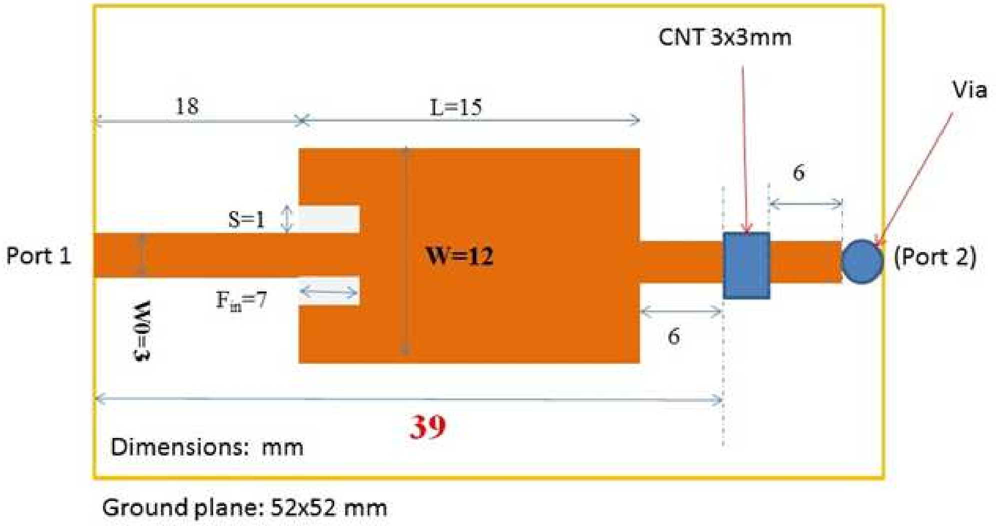

Figure 25. CNT stub loaded patch antenna scheme
https://www.mdpi.com/2311-5629/4/2/32/pdf

Moreover, the fabricated CNT loaded patch antenna is depicted in Figure 26.

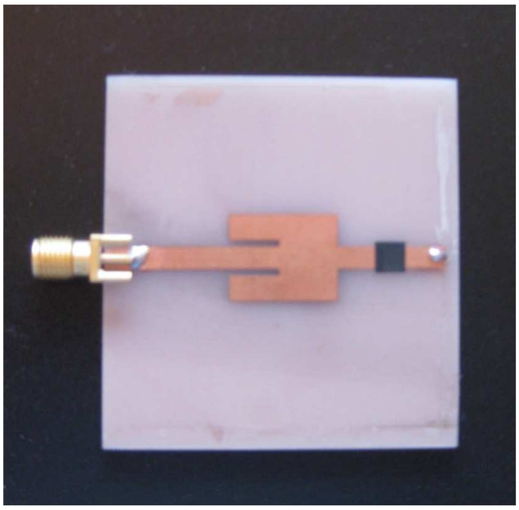

Figure 26. Fabricated CNT loaded patch antenna

The antenna schematic in HFSS is also shown in Figure 27.

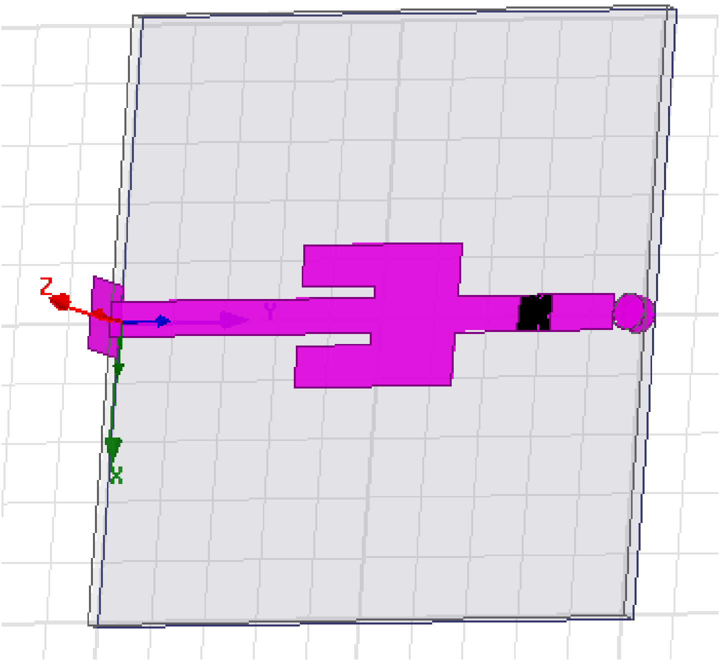

Figure 27. CNT loaded patch antenna schematic in HFSS

Regarding the Multi Wall carbon nanotubes (MWCNTs) size and position, the 2 or 3 layer CNT film with dimension of 3x3 mm has been inserted in the gap located at the center of the stub. Taking advantage of ANSYS HFSS full wave analysis, the CNT has been simulated as surface impedance which changes in various ambient and consequently results in shifting the resonance frequency of the patch antenna. Feed line is excited with a wave port and the stub terminated with a via hole connected to the ground plane.

4.2.1 Simulation and Measurement

As indicated previously, ANSYS HFSS is used to modeling the patch antenna. The simulation as well as the measurement includes 3 parts of patch only, patch plus stub and the CNT stub loaded patch antenna as shown in Figure 27. It is noted that CNT types which have been used in this project varies from 1 layer to 3 layer structure. Moreover, parametric simulation is done to show the effect of each parameter on the results in order to choose the best and proper value for them.

The reactance of the CNT film varies when expose to different ambient when its resistance remains constant; therefore, it is modeled by a resistance and variable reactance. The ground plane and patch are modeled as Perfect Electric Conductor (PEC). Regarding return loss, Figure 28 shows the agreement between the simulation and measurement for the reference antenna and for the 3 layer CNT stub loaded patch antenna as well. It is seen a frequency shift of 230 MHz from 4.36 GHz to 4.13 GHz in reference and CNT loaded antenna respectively. To be noted that the simulation results are obtained by considering the reactance of -1 KΩ for 3 layer CNT film. The difference in magnitude refers to the CNT film conductivity which is not estimated precisely.

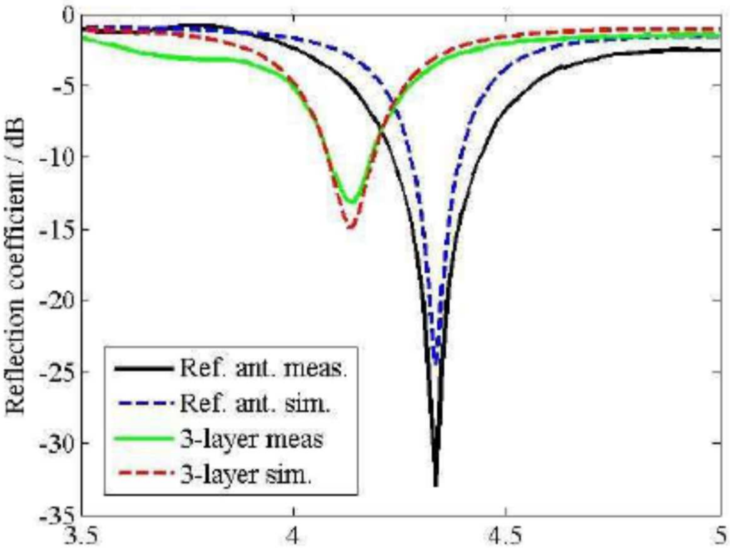

Figure 28. S11 measured and simulated results for reference and 3 layer CNT loaded antenna. https://ieeexplore.ieee.org/document/7481993

Other investigation is done by inserting 1 and 2 layer CNT thin films into the gap and changing the reactance of the surface impedance in simulation to see what happens. Figure 29 shows the results. It is crystal clear that there is an agreement between the measured return loss obtained from 3 layer CNT loaded antenna and the simulated result with the reactance of -1 KΩ.

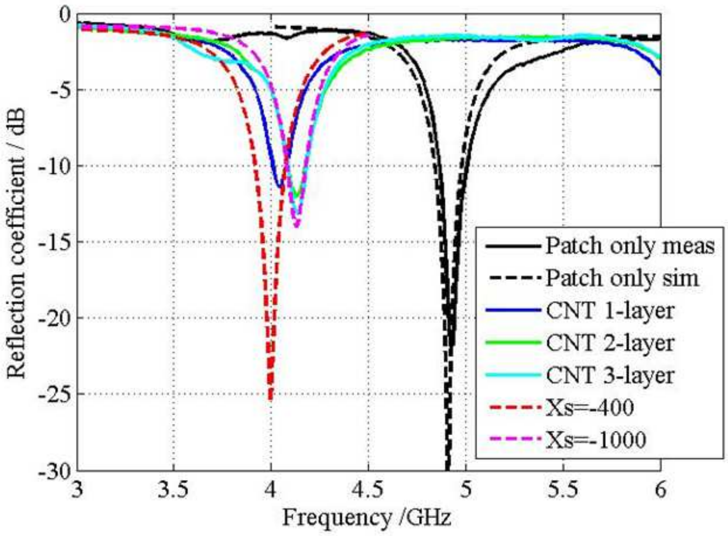

Figure 29. Measured and simulated S11 results for patch only and various CNT compositions

In case of using graphene sheet instead of CNT, the results are shown in Figure 30.

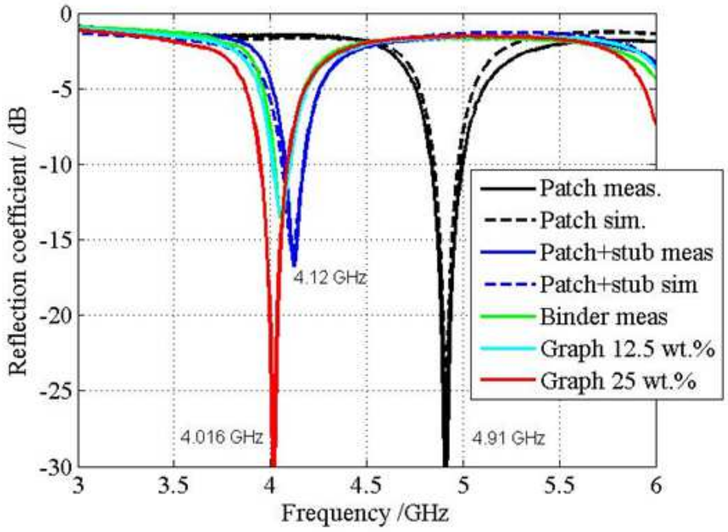

Figure 30. Measured and simulated S11 results for patch only and various graphene compositions.

As a matter of considering CNT or graphene sheet size effect on resonance frequency, Figure 31 shows that there is approximately 20 MHz positive shift in frequency from 4.022 to 4.039 GHz when the film size changes from 3×3 mm^2 to 4×3 mm^2 whereas almost 20 MHz negative frequency shift from 4.022 to 4 GHz is seen when the film size changes from 3×3 mm^2 to 4×4 mm^2 The most shifted frequency is related to the film of 4x4mm^2.

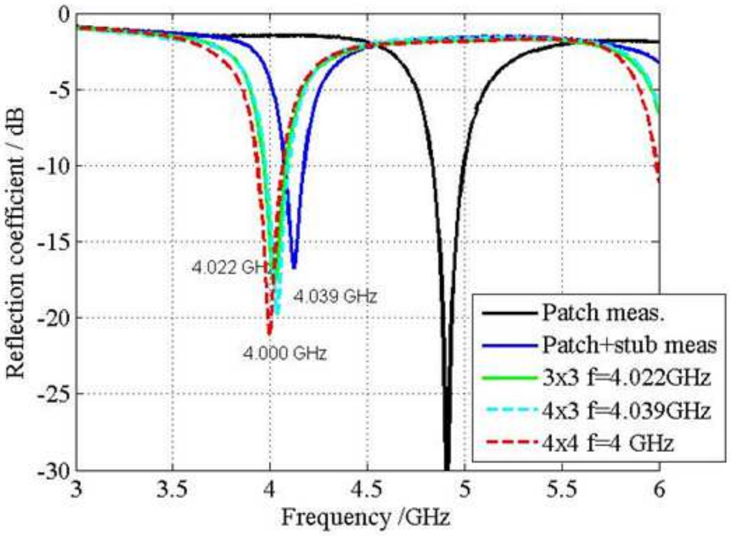

Figure 31. Parametric analysis on the film dimension

4.2.2 Radiation pattern and Gain

Taking advantage of an anechoic chamber with a double ridge horn (1-18 GHz), the radiation pattern is measured at a distance of 2.7 m. It is not observed a symmetric graph for the measured E-plane co-polarization pattern because of using coaxial cable as a feeding line. Moreover, cross-polarization is less than -22 dB in each plane. The agreement between the measurement and simulation is noticeable as shown in Fig Figure 32 and Fig Figure 33 for both the reference uncoated antenna and the CNT loaded 3 layer antenna. To be noted that the losses of the CNT film are not considered accurately in the simulation.

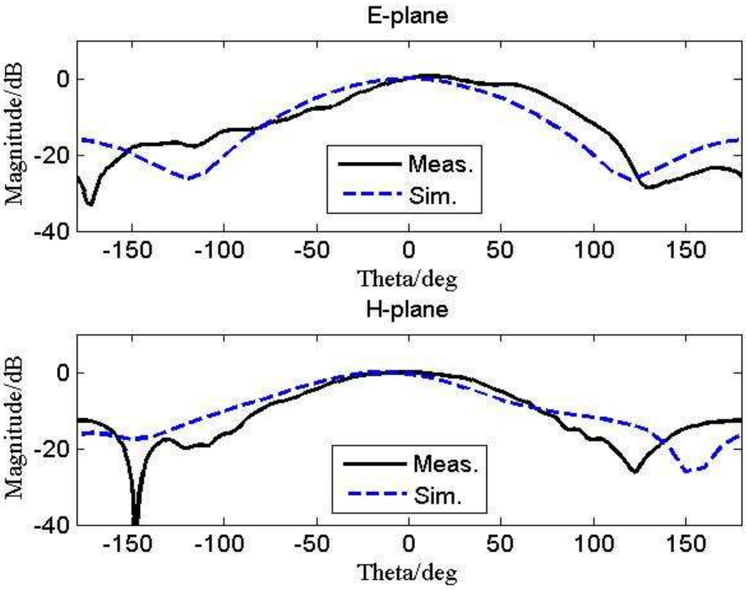

Figure 32. Measured and simulated radiation pattern (co-pol) of the reference uncoated antenna in the principal planes.
https://ieeexplore.ieee.org/document/7481993

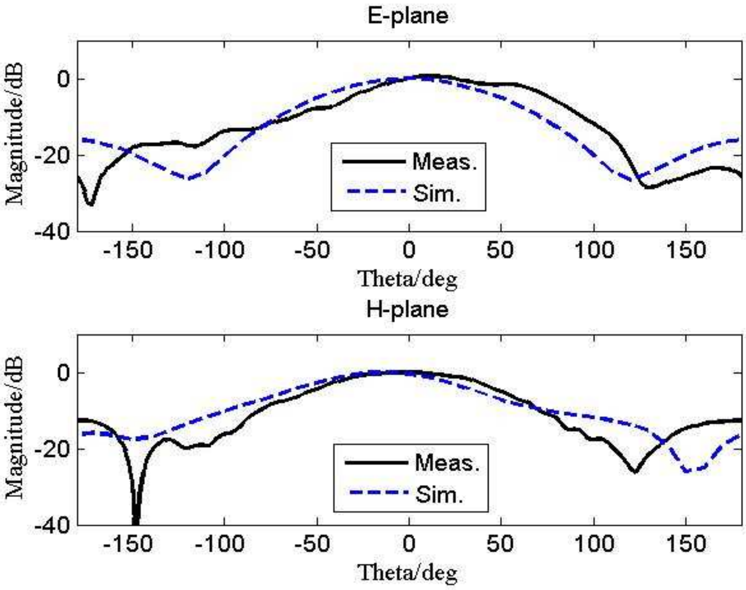

Figure 33. Measured and simulated radiation pattern (co-pol) of the CNT-loaded 3-layer antenna.
https://ieeexplore.ieee.org/document/7481993

In addition, the measured gain for 3-layer CNT loaded antenna is 2.9 dBi at 4.13 GHz while for unloaded antenna is 3.3 dBi at 4.36 GHz. The gains simulated in HFSS for the CNT stub loaded antenna is 2.85 dBi at 4.13 GHz whereas for the base patch+stub antenna is 3.88 dBi at 4.36 dBi. The whole results are shown in Figure 33-36.

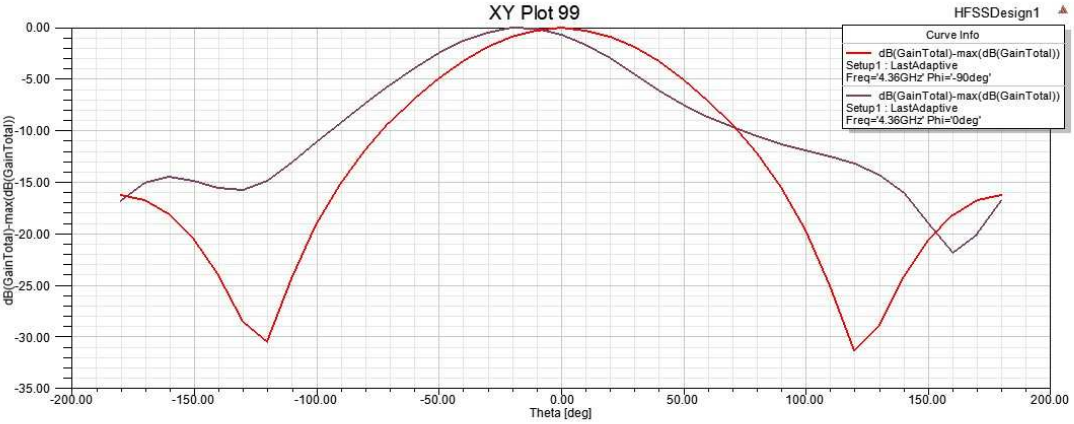

Figure 34. Normalized gain of patch+stub at 4.36 GHz.

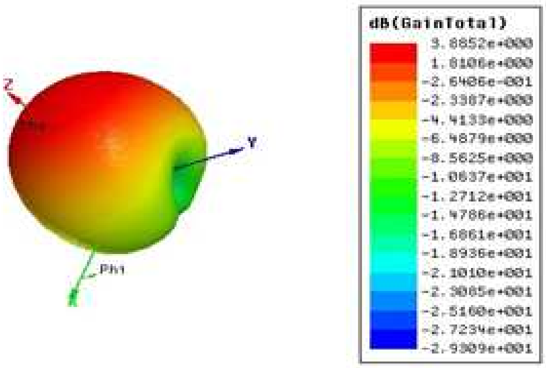

Figure 35. Gain of patch+stub at 4.36 GHz

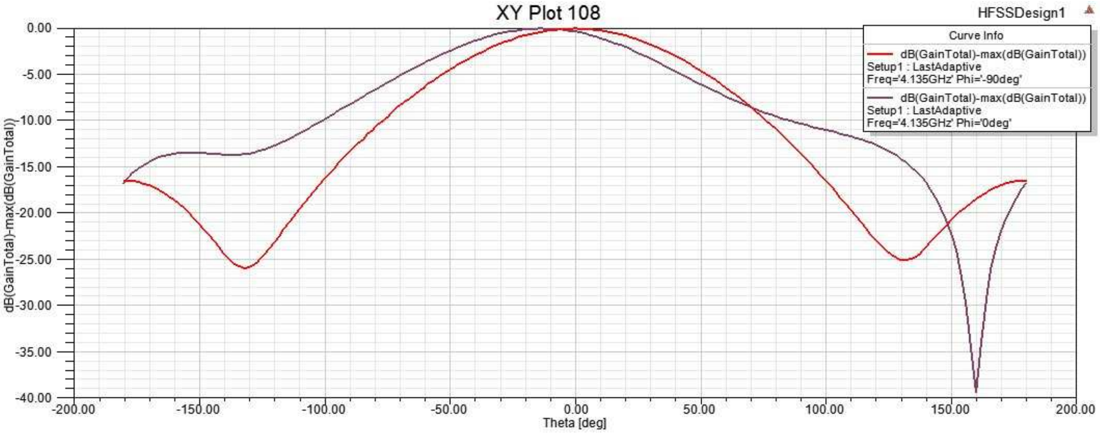

Figure 36. Normalized gain for CNT stub loaded antenna at 4.13 GHz

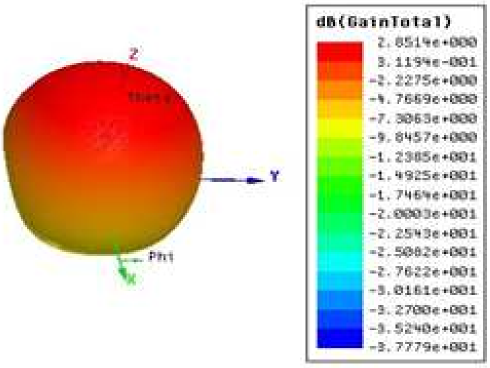

Figure 37. Gain of CNT stub loaded antenna at 4.13 GHz.

4.2.3 Parametric simulation

The new CNT loaded patch antenna under investigation is as Figure 38. The goal in this parametric simulation is focused on the reactance of the surface impedance which varies in different ambient while its resistance is fixed. To be memorized that the CNT or graphene thin film is simulated by a surface impedance in ANSYS HFSS.

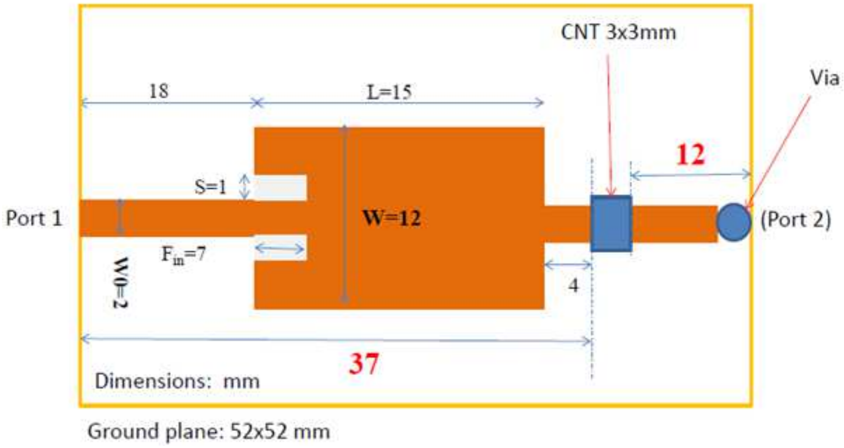

Figure 38. CNT loaded patch antenna- new design

The values used for substrate FR4 is as below:

- Relative permittivity ($\mathcal{E}_r$) = 4.4
- Loss tangent = 0.02
- Substrate thickness = 1.6 mm

The reactance of the surface impedance varies from 0 to -2000 when the resistance is fixed to 50 Ω. The comparison between the parametric simulations, patch only and patch plus 4 mm stub is shown in Figure 39. The results show that there is a considerable 492 MHz shift in resonance frequency from 4.183 to 4.675 GHz related to the reactance of 0 and -2000 respectively. This frequency shift can be sensed by a sensor to recognize the new ambient characteristics.

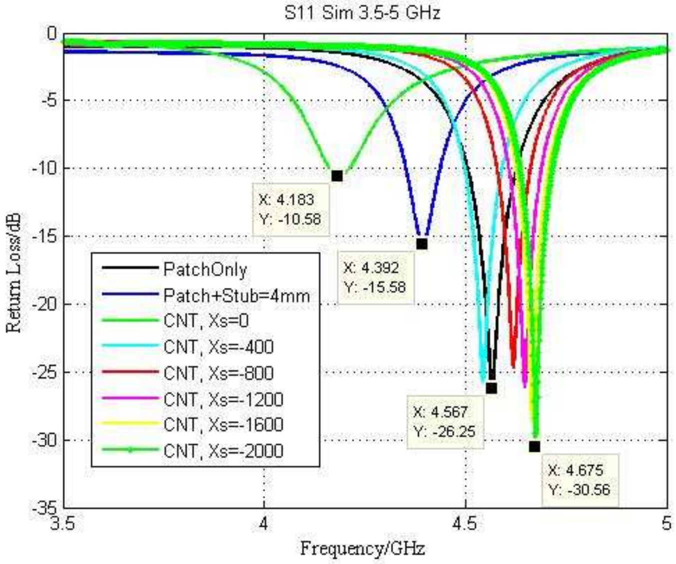

Figure 39. Parametric simulation of surface impedance sheet reactance

Gain is the other parameter under investigation when reactance of the graphene sheet varies. The simulations show that by varying the graphene sheet reactance from -400 to -2000 the gain increases as demonstrated in Figure 40 to Figure 42.

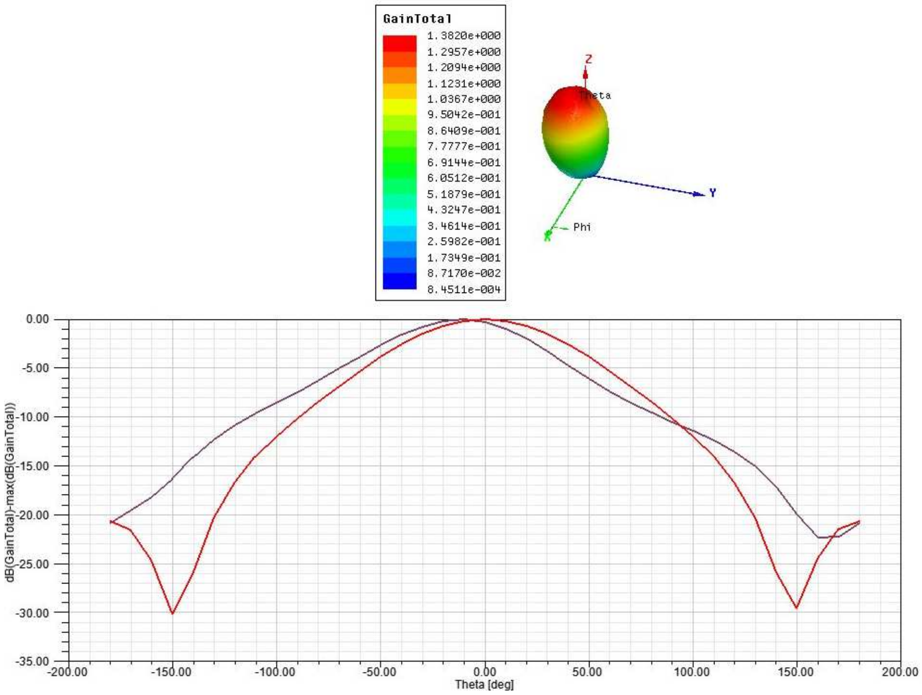

Figure 40. Gain at R=50 Ω &Xs=-400.

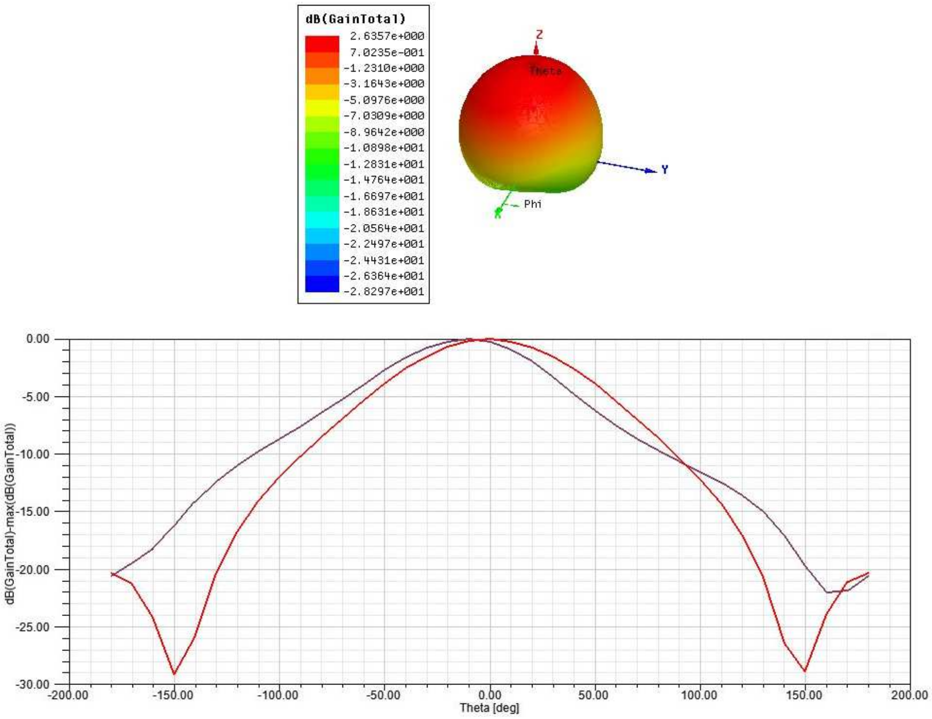

Figure 41. Gain at R=50 Ω & Xs=-1200.

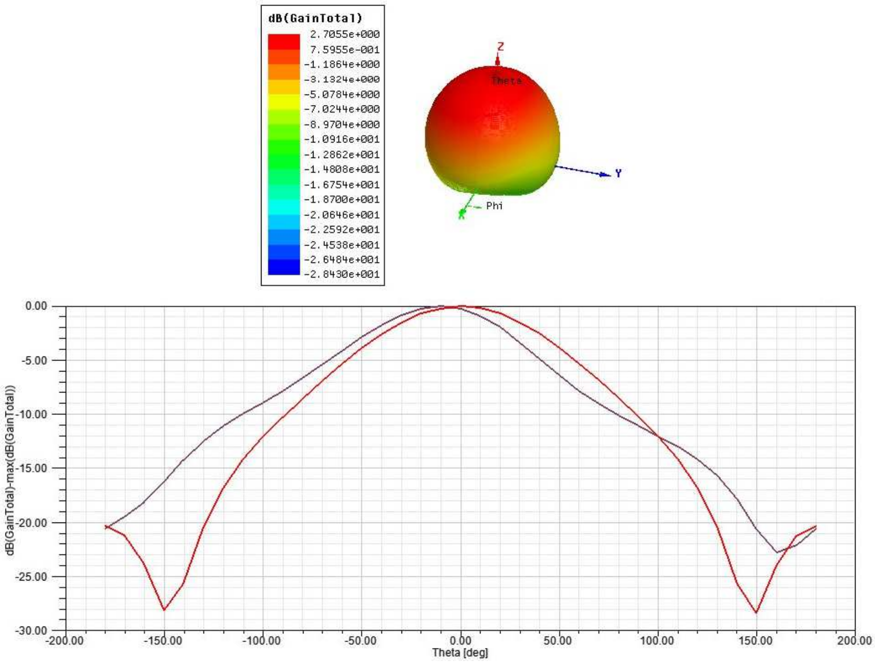

Figure 42. Gain at R=50 Ω & Xs=-2000.

4.3 Second prototype antenna

These prototype patch antennas resonate at around 2.4 GHz which is applicable for wireless communication.

4.3.1 Patch antenna with FR4 substrate

We go forward with the formulas in order to design a suitable patch antenna which resonates at 2.4 GHz:

$$\mathcal{E}_{eff} = \frac{4.4+1}{2} + \frac{4.4-1}{2}\left[1 + 12\frac{1.6}{38}\right]^{-\frac{1}{2}} \approx 4.08 \text{ ,}$$

$$L_{eff} = \frac{300}{2(2.4)\sqrt{4.08}} \approx 31mm$$

$$\Delta L = 0.412(1.6)\frac{(4.08+0.3)(\frac{38}{1.6}+0.264)}{(4.08-0.258)(\frac{38}{1.6}+0.8)} \approx 0.74mm \text{ ,}$$

L=30-2(0.74)≈ 28mm and W is set to 24 mm.

$$W_{feed} = \frac{7.48\times1.6}{e^{(50\times\frac{\sqrt{4.35+1.41}}{87})}} - 1.25\times0.035 \approx 3 \text{ mm}$$

Inset feed = 10 mm

The substrate and ground plane dimension are set to 75×65 mm. This design is shown in Figure 43.

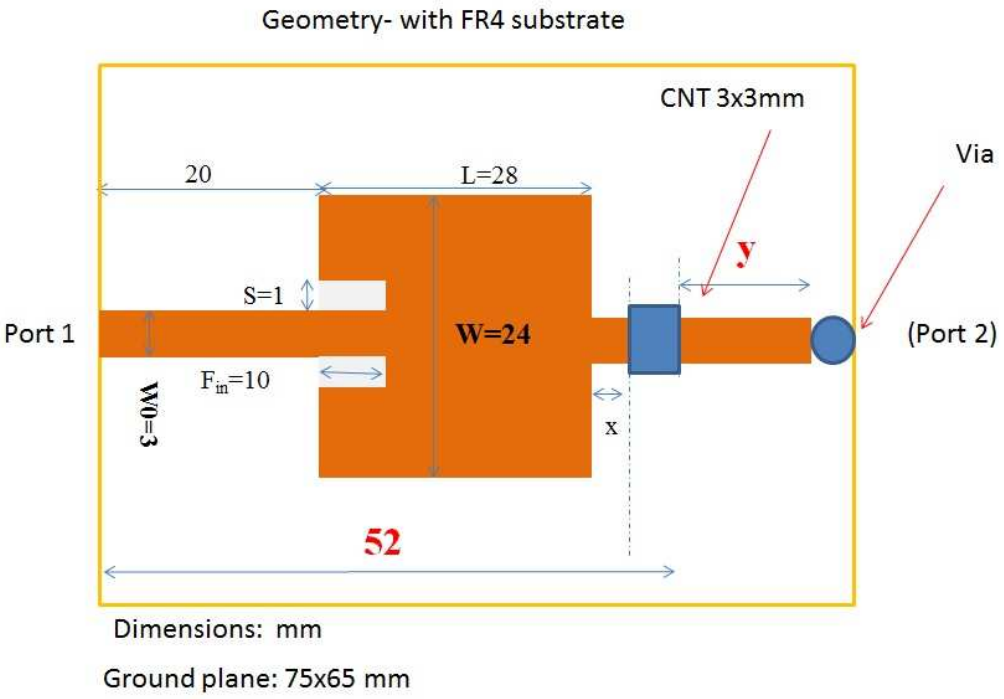

Figure 43. CNT loaded patch design at 2.4 GHz

4.3.2 Parametric analysis

Parametric analysis helps us to investigate the effect of each parameter separately and find the best values which meet our requirements.

Regarding parametric analysis for gap position, the following results are obtained:

- Patch only resonance frequency ≈ 2.56 GHz
- Patch + stub 8mm: resonance frequency ≈ 2.3320 GHz
- Patch+stub 8mm+CNT (Xs=-200): resonance frequency ≈ 2.21 GHz
- Patch+stub 5mm+CNT (Xs=-400): resonance frequency ≈ 2.432 GHz
- Maximum frequency shift (≈240 MHz) between the patch+stub and the CNT Xs=-200

Parametric analysis of gap position in the stub has been investigated and shown in Figure 44.

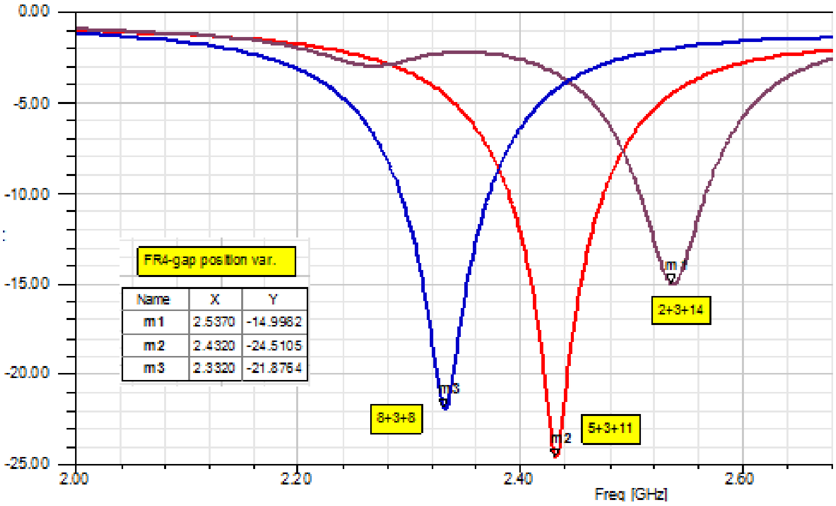

Figure 44. Parametric analysis of gap position with FR4 substrate

Stub width variation is another point which is worth considering. The case is composed of 5mm PEC+3mm CNT+11mm PEC. Just its width varies from 3 to 1 mm. It is seen that for the width of 3 mm we have better return loss of -25 dB.

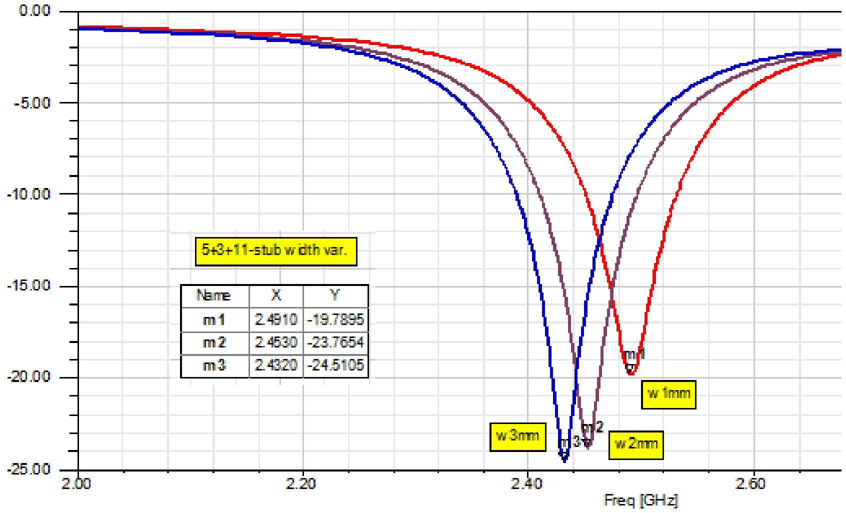

Name	X	Y
m1	2.4910	-19.7895
m2	2.4530	-23.7654
m3	2.4320	-24.5105

Figure 45. Stub width variation effects on results

Moreover, the dimension of the CNT film has an important role in shifting the frequency as well as the return loss magnitude. In this case its dimension impact is investigated when the impedance of CNT fixed at Z=50-i400.

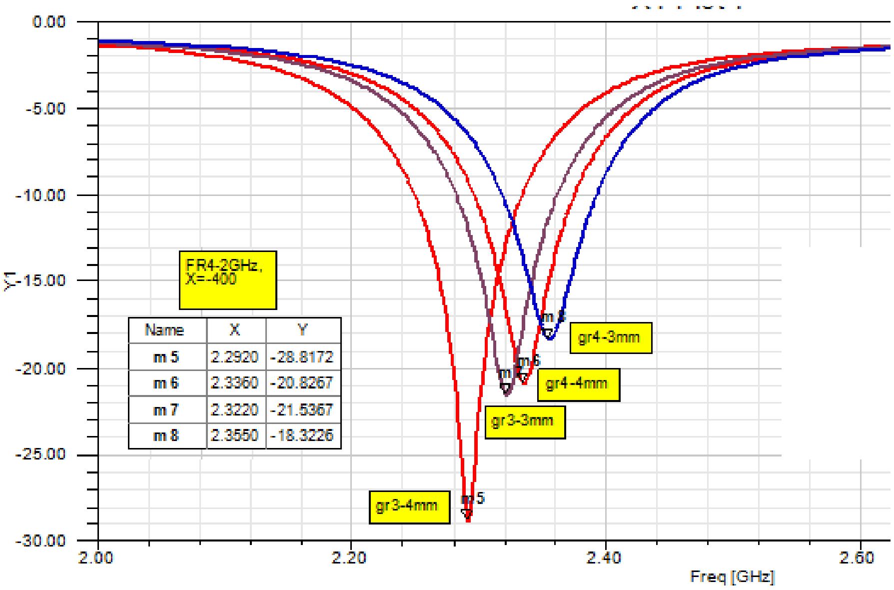

Name	X	Y
m5	2.2920	-28.8172
m6	2.3360	-20.8267
m7	2.3220	-21.5367
m8	2.3550	-18.3226

Figure 46. CNT film dimension effects on the results

Normalized gain also simulated at 2.4 GHz for E-plane as well as the H-plane.

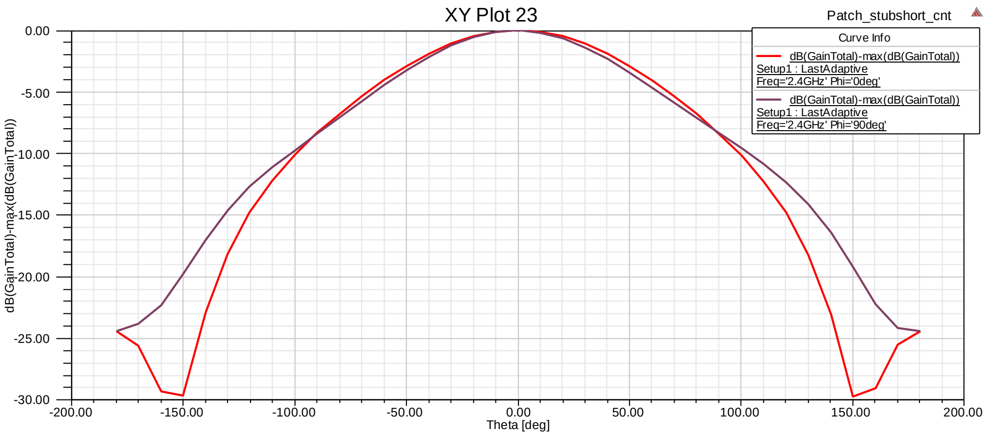

Figure 47. Normalized gain of CNT loaded patch antenna resonating at 2.4 GHz

4.4 Patch antenna with Arlon substrate

Arlon is the second substrate on which the design and simulations were focused. The Arlon has permittivity of 4.5, loss tangent of 0.0035 and thickness of 0.78 mm. To achieve the best return loss at resonance frequency of 2.4 GHz, which is so applicable in wireless communications, the design is as depicted in Figure 48. It is seen that the feedline width is reduced from 3 to 1.5 mm. The patch length and width are 29 and 38 mm respectively. Inset fed is set to 8 mm. The second stub is prolonged from 6 to 10 mm.

The calculations are as following:

$$W = \frac{300}{2(2.4)}\sqrt{\frac{2}{4.5+1}} \approx 38mm$$

$$\mathcal{E}_{eff} = \frac{4.5+1}{2} + \frac{4.5-1}{2}[1 + 12\frac{0.78}{38}]^{-\frac{1}{2}} \approx 4.32$$

$$L_{eff} = \frac{300}{2(2.4)\sqrt{4.32}} \approx 30mm$$

$$\Delta L = 0.412(0.78)\frac{(4.32+0.3)(\frac{38}{0.78}+0.264)}{(4.32-0.258)(\frac{38}{0.78}+0.8)} \approx 0.36mm$$

$$L = 30-2(0.36) \approx 29mm$$

$$w_{\text{feed}} = \frac{7.48\times0.78}{e^{(50\times\frac{\sqrt{4.5+1.41}}{87})}} - 1.25\times0.035 \approx 1.5 \text{ mm}$$

Inset feed = 8 mm

The substrate and ground plane dimension are set to 60×55 mm. The design is shown in Figure 48.

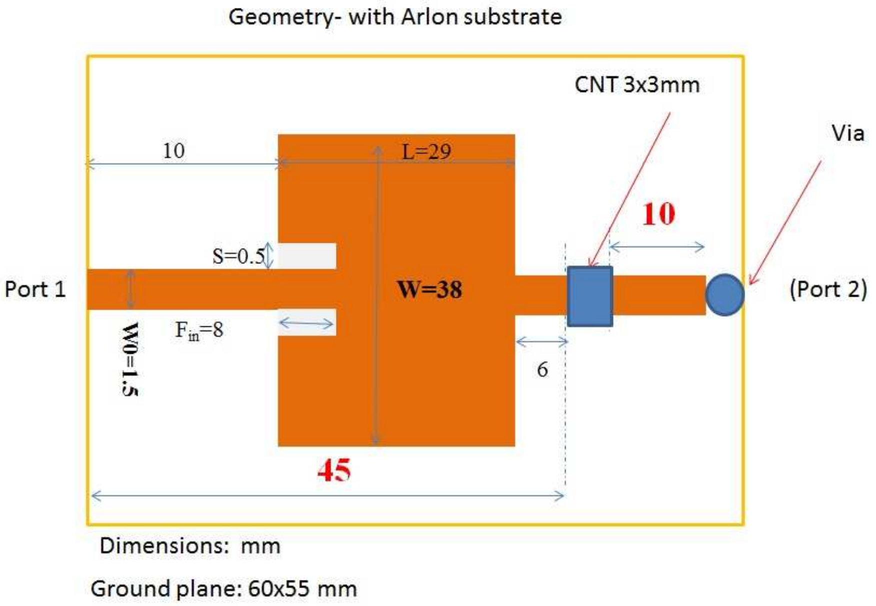

Figure 48. CNT loaded patch antenna with Arlon substrate

It is observed from simulation of the patch alone, patch plus stub 1mm as a reference point and patch plus stub CNT loaded patch antenna that the frequency shift by inserting the CNT film (Z=50-i200) is decreased by 80 MHz which can be sensed and used as a sensor**.**

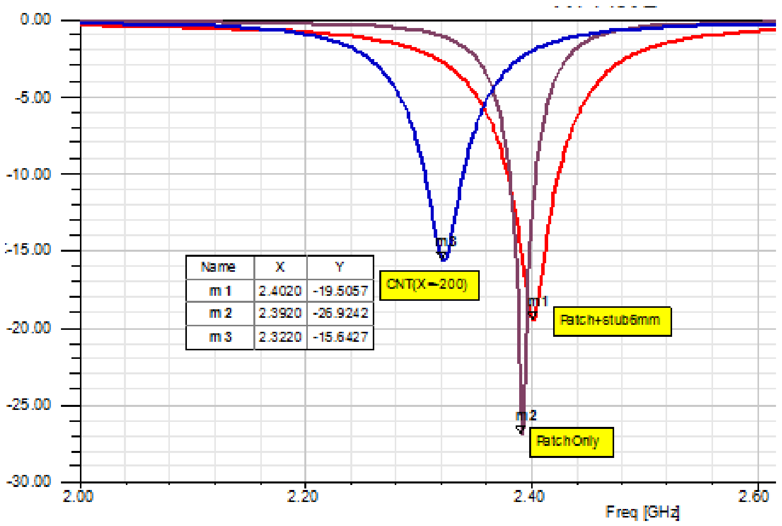

Figure 49. Simulation results of the antenna with Arlon substrate

Normalized gain also simulated at 2.4 GHz for E-plane as well as the H-plane.

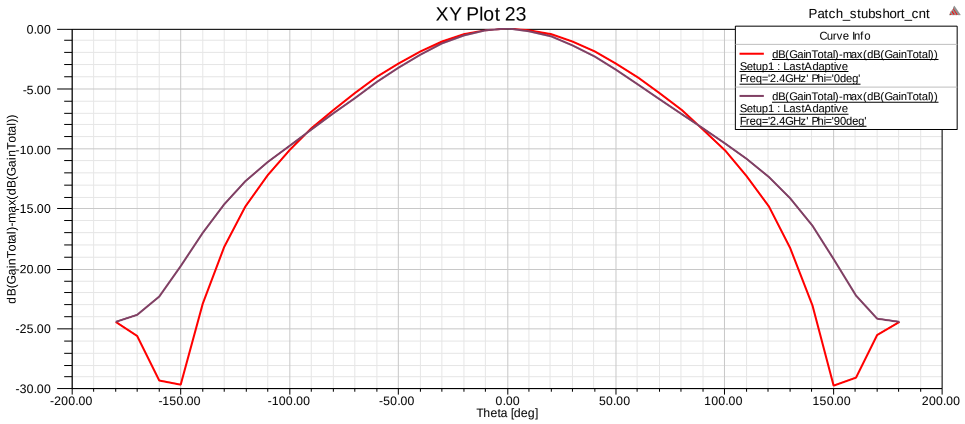

Figure 50. Normalized gain of CNT loaded patch antenna with Arlon substrate resonating at 2.4 GHz

Chapter 5

5. Aperture Coupled Patch antenna

Carbon nanomaterials like carbon nanotubes (CNTs) and graphene, in favour of the fast progress in nanotechnology, are being vastly used in sensor applications profiting from their noticeable carrier mobility, large surface area/volume ratio, adjustable surface chemistry, and the ability to operate at ambient temperatures. By integration of the CNT chemical detector comprising a thin-film or thick-film passive circuit element (such as planar resonator or capacitor on a dielectric substrate), with radio frequency (RF) antennas, nanotechnology has the potential to be used in the development of ubiquitous wireless sensor networks. Based on its application, it is beneficial to use these wireless points in fixed or moving positions for monitoring hazardous chemicals as well as the environmental pollutants and its effects on health, for instance. The antenna can work in multiple transmit/receive modes to make the detected data transfer between various sensor nodes.

Previously, CNTs have been incorporated directly in antenna structure of the sensor. In this case, the performance is degraded because of CNT films losses. As a consequent, radiation efficiency is weakened at the communication frequency of the sensor. To reduce the impact of these losses, the CNT film shall properly integrate with the antenna in a way that does not affect the antenna radiation performance as well as the sensor efficiency at the presence of the antenna. This goal can be reached by minimizing the coupling between the sensor and antenna element. In order to reducing this coupling effect, an aperture coupled patch antenna, which the CNT thick film sensor is inserted in its feed line, is used. In this regard, two types of the antenna are deployed. First, the CNT film deposited at a gap located in the extension of the feed line. Second, design and incorporating InterDigitated Capacitor (IDC) into the feed line in order to meet the requirements of sensing and antenna impedance matching as well.

5.1 Aperture Coupled Patch antenna Design

Aperture Coupled Antenna has 3 layers including the microstrip feed line, ground plane with coupling aperture, antenna substrate and radiating patch as shown in Figure 51.

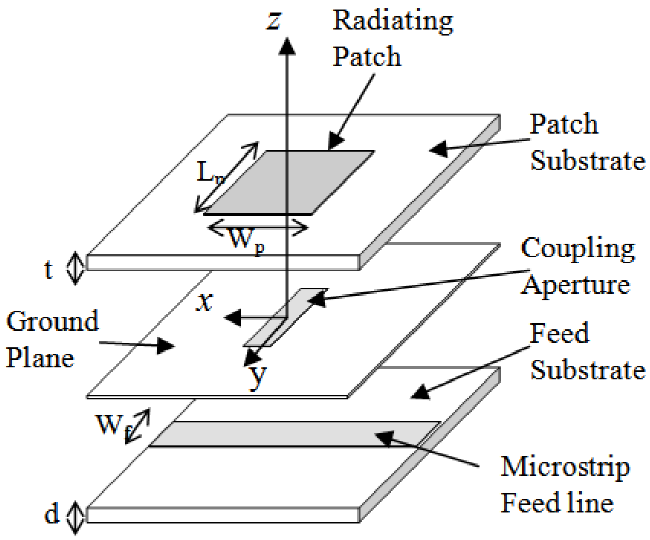

Figure 51. Layers of Aperture Coupled Patch antenna
https://www.researchgate.net/publication/268357579_Large_aperture_coupled_microstrip_patch_antenna_arrays_proposal_for_the_opto-electronic_control_of_micro_and_mm-wave_radiation/figures?lo=1

The open circuit terminated feed line, simulated in HFSS, should have the length of 0.739λ. The center of aperture has 0.211λ distance from the end of feed line as depicted in Figure 52. According to the open circuit transmission line, the voltage is 0 and the current is maximum at the distance of λ/4. Considering the effects of patch loading and ground aperture, this distance is reduced to 0.211λ.

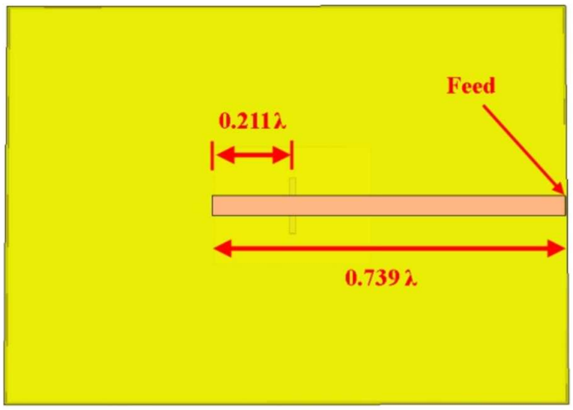

Figure 52. Feed line dimensions in aperture coupled antenna
https://pdfs.semanticscholar.org/f36e/6547818f642c26c92b9c9a1507b1ad3e3624.pdf

For instance, we start to design an aperture coupled patch antenna to work in ISM 2.4 GHz band. Two different dielectric layers are being used in its structure; the antenna substrate (Rogers

RO3010) on the top with dielectric constant of 10.2, tan δ = 0.0035, thickness of 1.6 mm, and the feed substrate (Rogers Ultralam 1250) on the bottom with dielectric constant of 2.54, tan δ = 0.0015, and the same thickness.

The geometry of feed and patch layer is shown in Figure 53 and Figure 54.

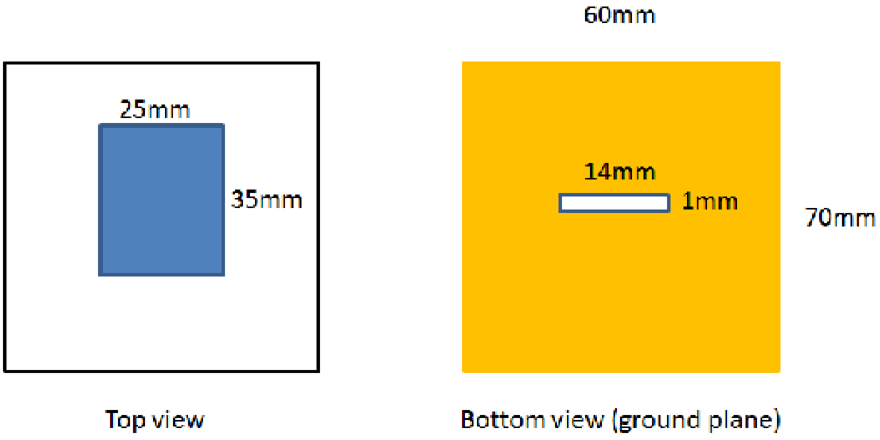

Figure 53. Patch layer geometry

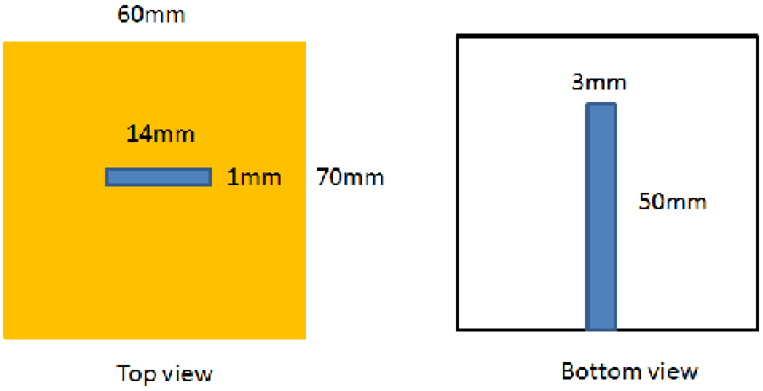

Figure 54. Feed layer geometry

The estimated dimensions for slot length and width are 0.148λand 0.016λ respectively. In addition, the feed substrate height is set to 0.0169λ. the whole dimensions are indicated in Figure 55.

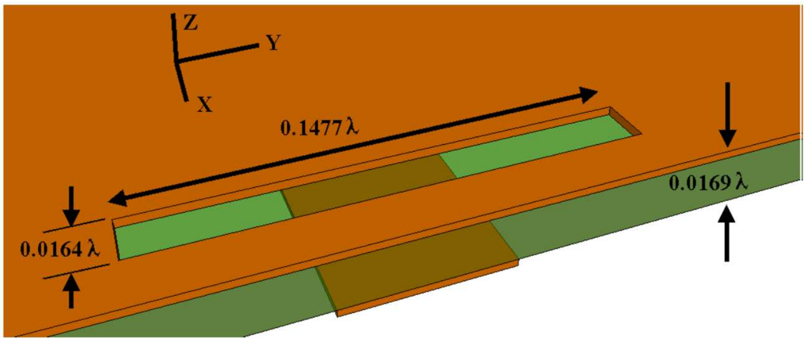

Figure 55. Feed substrate and slot dimensions
https://pdfs.semanticscholar.org/f36e/6547818f642c26c92b9c9a1507b1ad3e3624.pdf

Regarding the simulation in HFSS, the model is shown in Figure 56.

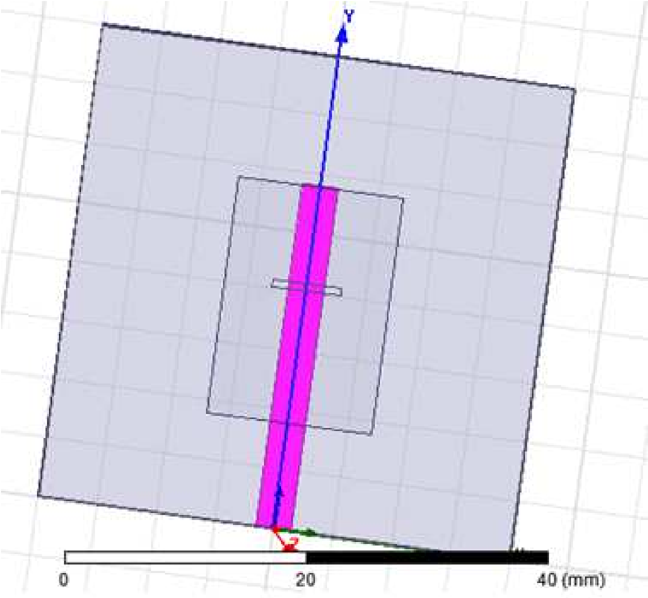

Figure 56. Aperture coupled patch antenna HFSS model

The return loss of -47 dB at 2.45 GHz shows that it would be good alternative to use in wireless applications. The S11 simulated result is depicted in Figure 57.

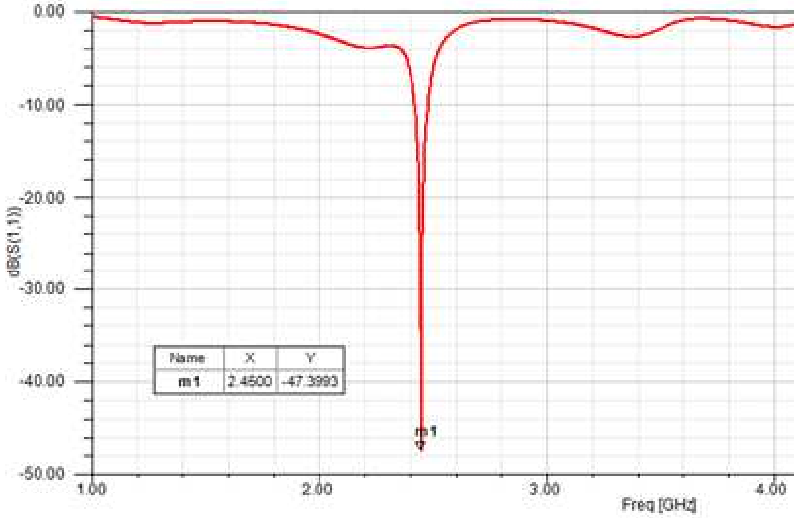

Figure 57. Return loss of the aperture coupled patch antenna

5.2 ACP CNT loaded antenna Design

Previously, a wireless gas sensor has been realized by incorporating single walled carbon nanotube thin film in patch antenna [14], [21] and the CNT film surface was made to have maximum sensibility to ammonia [8]. The chemical reaction of exchanging charge carriers between the CNTs and gas makes RF impedance change in relevant circuit. The loaded CNT film changes the resonant frequency of the antenna whenever exposes to gas. This frequency shift is the important factor in measuring the sensor response [36-38]. In spite of a considerable shift in frequency, the radiation is degraded strongly by the loaded CNT film in series with the patch. Therefore, it is necessary to design a good structure in order to minimize the series loading effect in order to improve the radiation efficiency. The aperture coupled seems to be a proper choice to resolve this problem. Because the feed line current is isolated from the antenna current by a slot aperture placed in ground plane. By inserting the CNT film at the end of the feed line on microstrip gap or IDC, the coupling between the feed line with connected sensor and aperture coupled antenna is minimized; therefore, there is no impact on radiation and gain of antenna as well as the sensing behavior.

First, inserting CNT film directly at the end of feed line is taken into consideration. The aperture coupled patch antenna, as before, resonates at 2.45 GHz. The feed substrate is Rogers RO3010 with thickness of 1.6 mm, permittivity of 10.2 and patch substrates and loss tangent of 0.0035. The patch substrate is Rogers Ultralam 1250 with thickness of 1.6 mm, permittivity of 2.5 and loss tangent of 0.0015. The geometry of Feed line CNT loaded ACP antenna is shown in Figure 58.

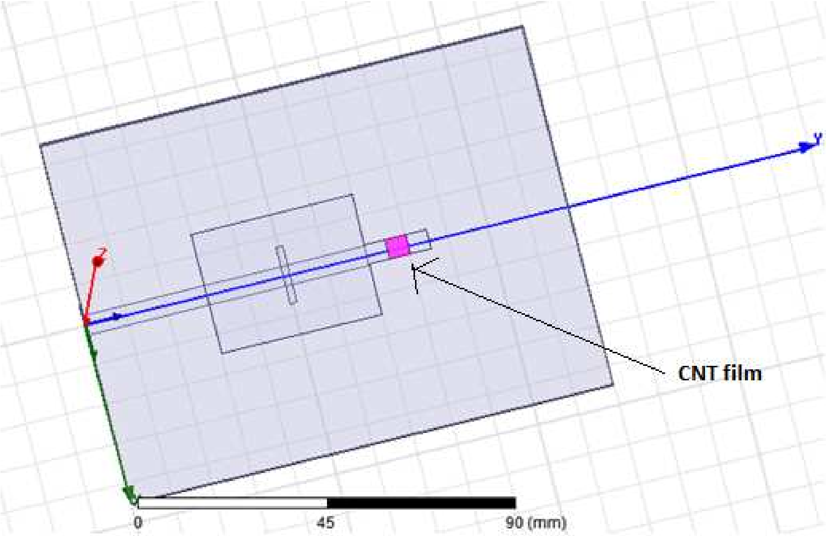

Figure 58. CNT loaded ACP in HFSS.

To be noted that the stub included 4 mm copper+ 3 mm CNT + 4 mm copper and CNT film size is 3×3 mm^2. The return loss simulated for different values of the surface impedance as below:

- R=0.5 Ω, X=-15
- R=20 Ω, X=-100
- R=1000 Ω, X=0

Figure 59 shows the relevant simulations in HFSS.

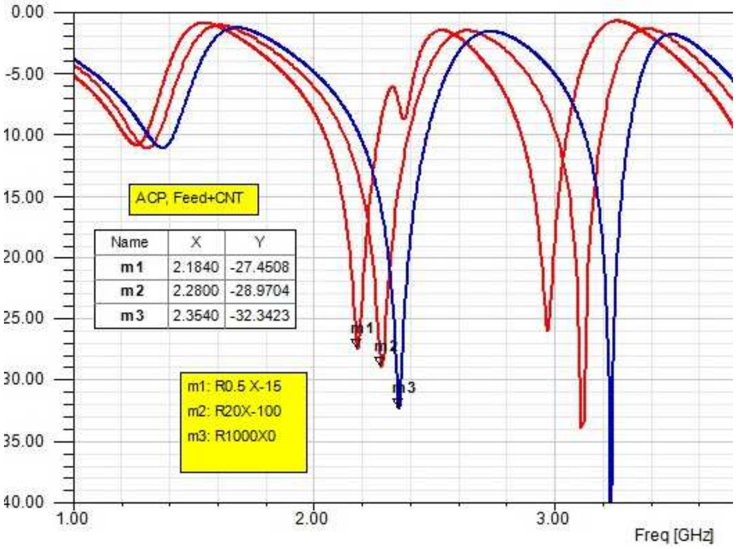

Name	X	Y
m1	2.1840	-27.4508
m2	2.2800	-28.9704
m3	2.3540	-32.3423

Figure 59. Return loss simulation for various resistance and reactance of the surface impedance

Table 2. Surface impedance effect in ACP

Configuration	Resonance Frequency (GHz)	Return loss (dB)	Frequency shift (MHz)
Feed+stub+cnt+stub R=0.5, X=-15	2.18	-27.45	270
ACP only	2.45	-47.4	Reference point
R=20, X=-100	2.28	-29	170
R=1000, X=0	2.35	-32.3	100

Table 2 implies that whenever the resistance increases, the resonance frequency shift from the reference point is decreased. To be noted that the resonance frequency shift is occurred when the ambient is changed and can be sensed by a sensor for realizing the ambient characteristics.

5.3 ACP configuration with InterDigitated Capacitor (IDC)

As already mentioned, InterDigitated Capacitor (IDC) is added in extension of the feed in order to have a better impedance match between the feed line and the patch. Moreover, inserting the CNT film into IDC results in meeting our sensor application needs.

The ACP with IDC configuration is designed to work in ISM 2.4 GHz band. Two dielectric layers are being used in its structure; ; the feed substrate (RT Duroid 5880) on the bottom with dielectric constant of 2.2, tan δ = 0.0009, thickness of 0.762 mm, and the antenna substrate (Rogers RO3010) on the top with dielectric constant of 10.2, tan δ = 0.0035, and the thickness of 0.508 mm. A thin slot located in ground plane in the middle has the role of coupling between the two mentioned parts.

The dimensions of the ACP are shown in Figure 60 and Figure 61. The dimensions (in mm) of the patch are given by L_P= 35 and W_P= 25. The slot has L_S= 14, W_S= 1 when both the substrates have L_{sub}= 80, W_{sub}= 75 and the feed line has L_f= 50, W_f= 0.5 for 50 Ωs impedance.

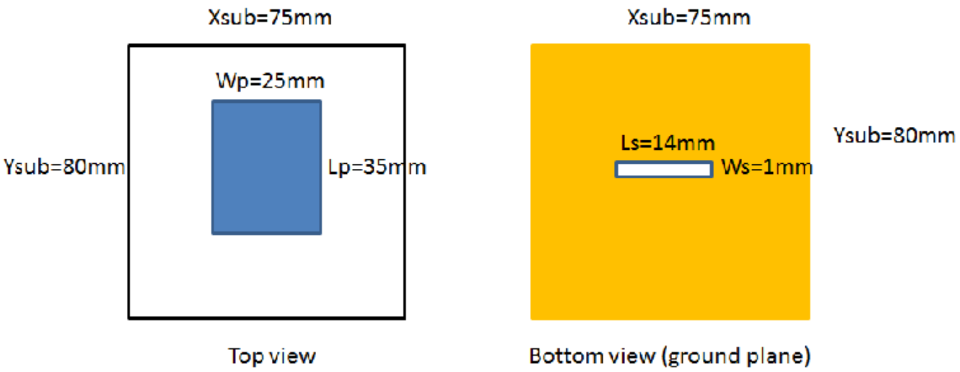

Figure 60. Patch layer geometry

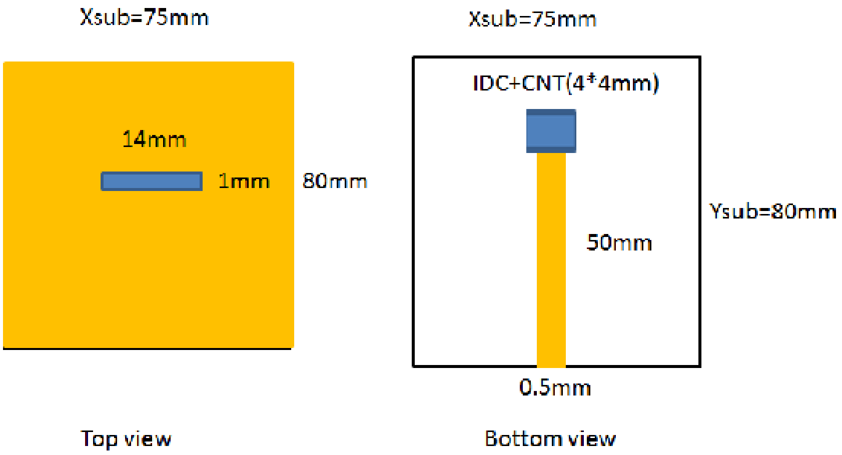

Figure 61. Feed layer geometry

As shown in Figure 62, an IDC of surface area 5.0 × 5.8 mm^2 with 10 interleaved fingers, five on each side, each of width 0.4 mm and inter-digit spacing of 0.2 mm, is connected at the end of the microstrip feed line. The connection pad joining all the fingers on one side has the dimensions 5.8 × 0.4 mm^2. The novelty of this ACP is using IDC at the end of its feed line in order to accommodate the CNT thick film and consequently add the sensing application to the antenna. The CNT film which works as a sensor, is simulated by a surface impedance comprising a parallel RC circuit, with R being the resistance of the CNT film (usually very low due to high conductivity of CNTs) and the capacitance C resulting from the shunt reactance of the film and the IDC geometry.

Fig 5.13 shows the ACP antenna with IDC simulated in HFSS.

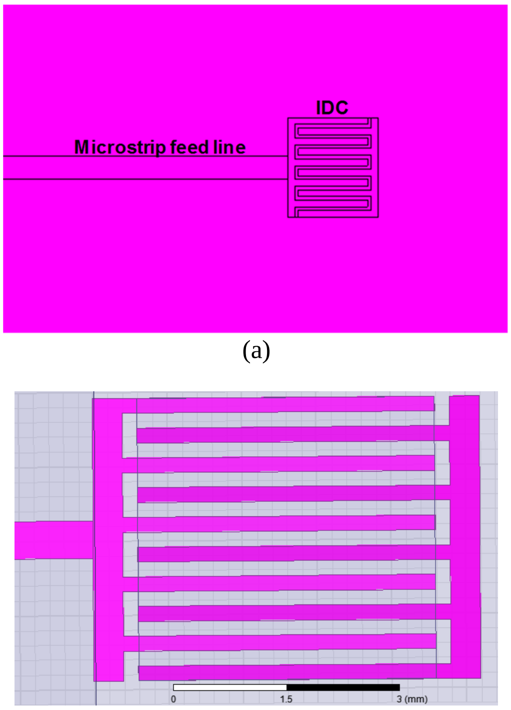

(a)

(b)

Figure 62. (a) Proximity-coupled feed line with IDC connected in series. (b) The simulated 10 fingers IDC in HFSS.

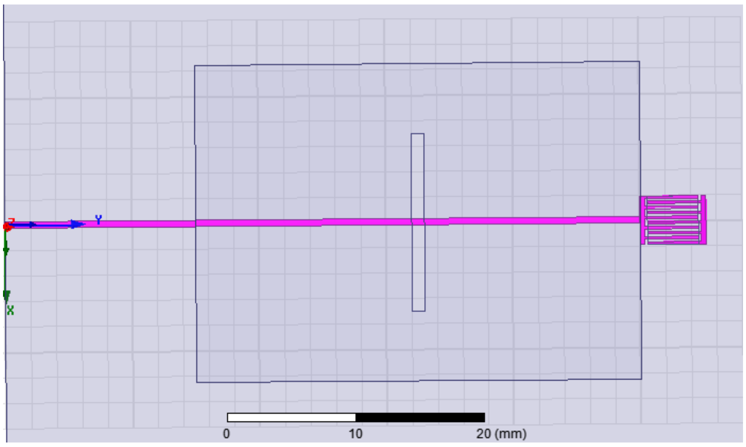

Figure 63. HFSS model of ACP antenna with IDC

5.4 Simulation Results

Simulation first goal is to find the suitable dimensions for IDC in order to have the minimum return loss (S11) at 2.45 GHz. It is found that the IDC size of 4×5.8 mm^2 results in -22 dB return loss at 2.45 GHz (fig 5.14). Second, the CNT film is deposited on the IDC and parametric simulation has been done on its surface impedance to assess its effect on the antenna efficiency. The shunt resistance is set to 100 and 1000 Ωs per square. The simulations show that resistance change solely does not have any strong influence on resonant frequency and the return loss value as well.

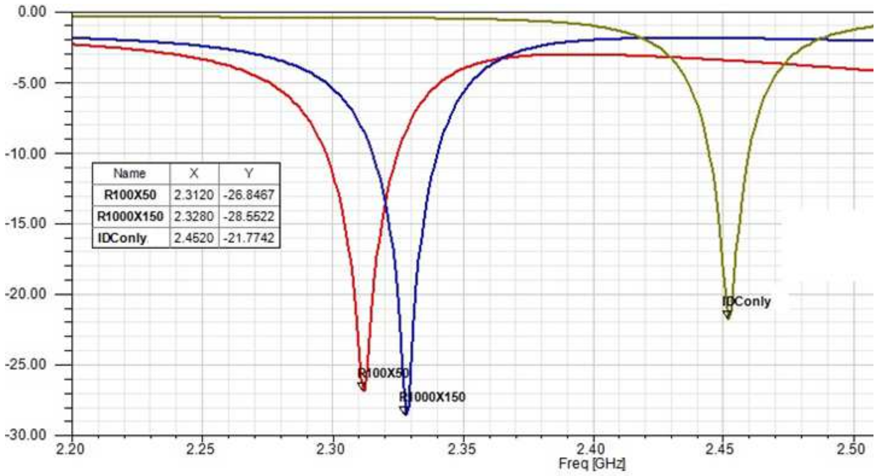

Figure 64. Return loss of the ADP_IDC patch sensor as a function of the film impedance.

Shut capacitance, in contrary, has impact on both the resonant frequency and return loss. Therefore, impedances of 100-j50 and 1000 j-150 have been taken into consideration. Four probe impedance measurement is used to measure surface impedance on MWCNTs [8]. It is obvious that the return loss not varies significantly when we used IDC sensor film structure in ACP and remains as low as -22 dB. As indicated in Table 3, frequency shifts are 120 and 140 MHz for impedances of Z=1000-j150 and Z=100-j50 respectively.

Table 3. Surface impedance effect in ACP with IDC

Configuration	**Resonance Frequency (GHz)**	**Return loss (dB)**	**Frequency shift (MHz)**
ACP + IDC only	2.45	-22	Reference point
ACP+IDC+CNT R=100, X=-50	2.31	-27	140
R=1000, X=-150	2.33	-29	120

Figure 65 shows the radiation pattern for the loaded ACP IDC with CNT film. The simulated gain is 6.6 dB at 2.3 GHz and the CNT surface impedance is Z=100-i50.

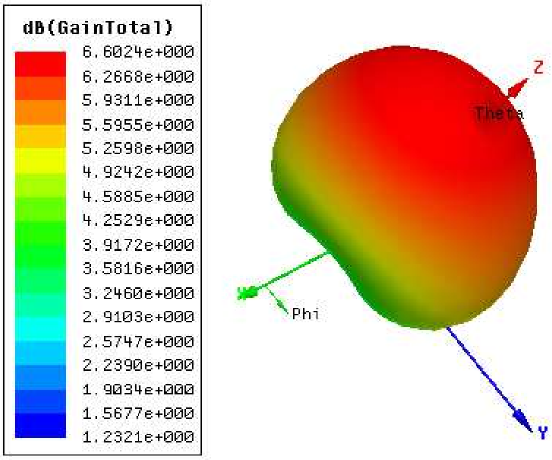

Figure 65. Gain for the loaded ACP IDC with CNT film.

Chapter 6

6. Microwave Ring Resonator

6.1 A copper-clad slotted Ring Resonator Design

In this chapter, a copper-clad slotted ring resonator is designed and fabricated on 0.79 mm thick FR-4 substrate (dielectric constant of 4.3 and loss tangent of 0.03) with a microstrip proximity-coupled feedline of length 17 mm. The size of the substrate is 35×35 mm^2.

First, a slotted ring without the graphene film is designed to resonate at 2.45 GHz (inner radius $R_i = 12.7$ mm, slot width $W_s = 0.5$ mm) as shown in Figure 66. The slot line mode is excited by proximity-coupling with the 50 Ω microstrip feed line.

6.2 Graphene loaded slotted Ring Resonator Design

In order to examine the resonant response of the loaded ring, graphene films of size 3×3 mm^2 and either 25% or 33% in weight concentrations are sequentially inserted along the ring at 90° and 180°, clockwise with respect to the feed line at 0°, and full-wave electromagnetic simulations are performed by modeling the graphene film at the resonant frequency as a surface impedance. Due to circular symmetry, only the film locations 90° and 180° are of interest. A film cannot be deposited at 0° as it interferes with the slot excitation field resulting from the feedline. Furthermore, the film at 90° location produces the cross-polarized or orthogonal resonant mode of the same characteristics as the fundamental mode obtained with the 180° film orientation, and therefore, is not considered.

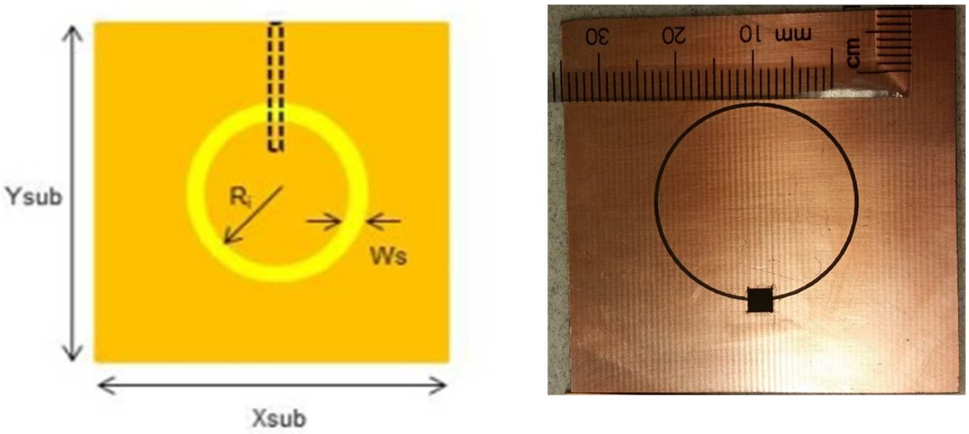

Figure 66. The slotted ring resonator and its realization with graphene thin film deposition.

6.3 Simulation and measurements

Both loaded and unloaded configurations of the slotted ring resonator are characterized at microwave frequencies by measuring the reflection coefficient at the feed port using a Vector Network Analyzer (Agilent E8361A). These resonators have been designed and simulated in CST Microwave Studio and ANSYS HFSS with the graphene film modeled as a surface impedance. To be noted that the full-wave 3D simulation in CST and HFSS captures all the electromagnetic and parasitic coupling effects.

The simulated graphene loaded and unloaded ring resonator is shown in Figure 67. Tangential Electric field for the base line ring resonator is also depicted in Figure 68.

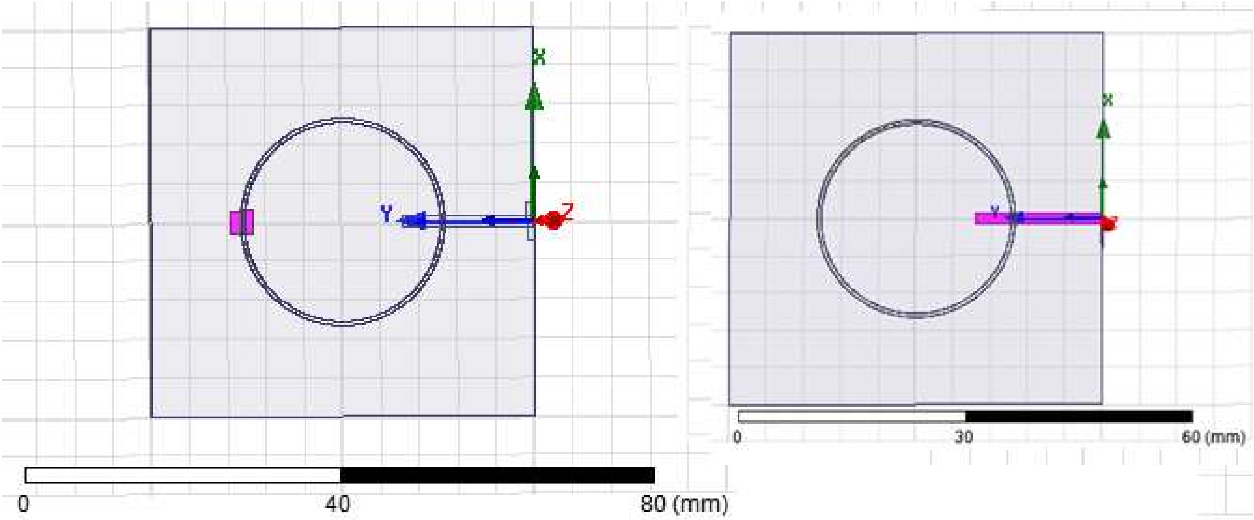

Figure 67. Graphene loaded and unloaded ring resonator models in HFSS.

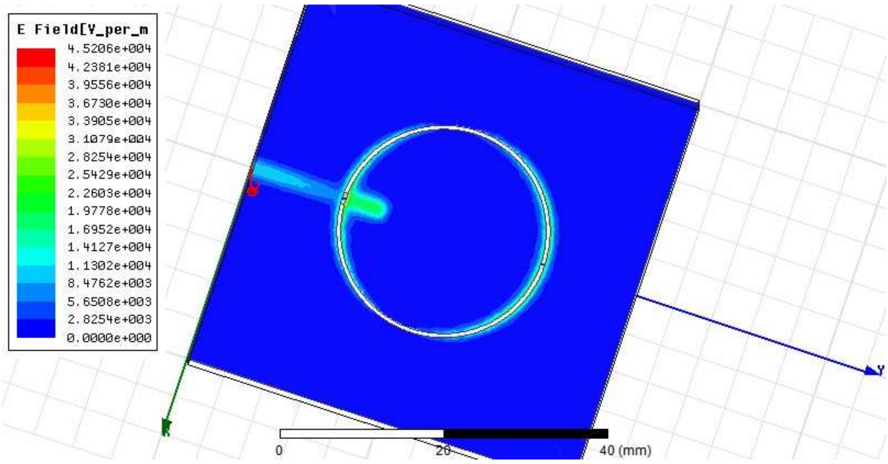

Figure 68. Tangential E field in base line ring resonator at 2.47 GHz.

The unloaded ring is measured first, and it shows a resonance at 2.47 GHz. This is the baseline geometry used to study the effects of graphene films. Excellent agreement is observed between the measured and simulated results in Figure 69 for the unloaded ring. Next, a graphene film 33% in weight with size of 3×3 mm^2 is inserted across the slot in the ring resonator, diametrically opposite to the feed at the location 180°, and the return loss of the loaded resonator is measured. A good agreement between simulated and measured data is also observed for the loaded film configuration in Figure 69.

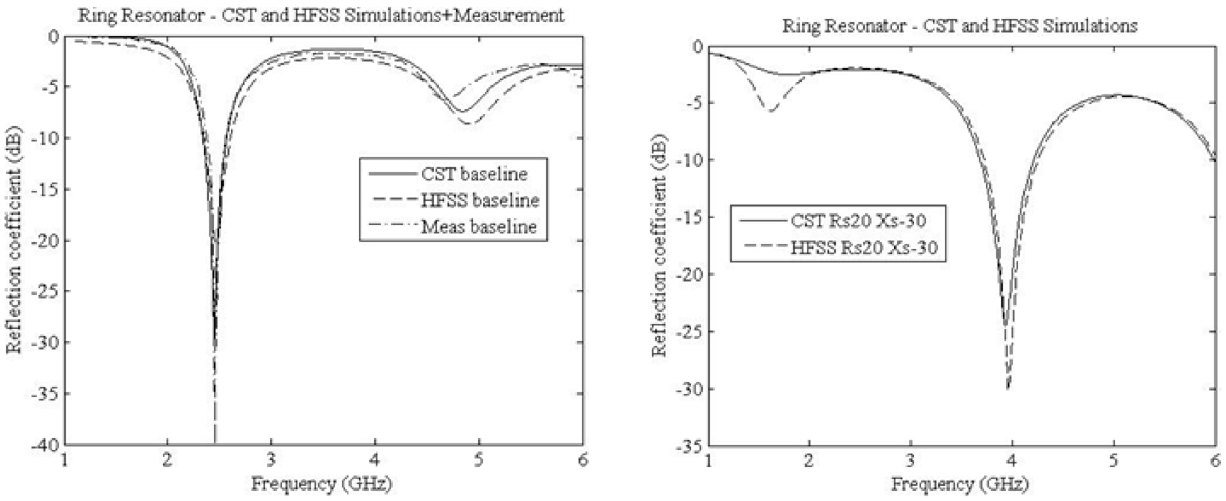

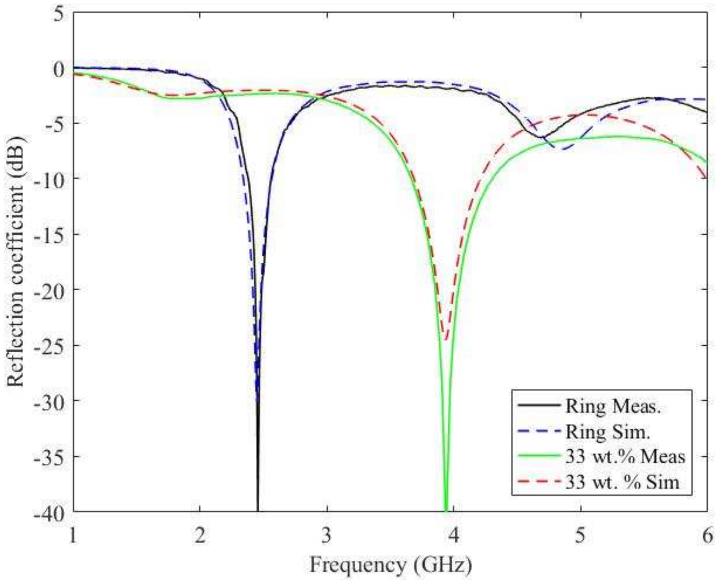

Figure 69. Base line and Graphene loaded ring simulations and measurements.

6.4 Equivalent Circuit Model of graphene film

Since the graphene film is deposited over the slot gap, the equivalent circuit of the film is a parallel RC circuit, as discussed in Chapter 3. The capacitance due to graphene film is very small and the conductivity, inversely proportional to the sheet resistance, is the most important parameter of interest in RF characterization of the graphene film. For the parallel RC circuit, the admittance is given by

$$Y = {}^{1}\!/_{R} + j\omega C. \tag{9}$$

The impedance is then

$$Z = \frac{1}{Y} = Z_R - jZ_I = \frac{R}{\Delta} - \frac{R(\omega RC)}{\Delta} \tag{10}$$

$$\Delta = 1 + (\omega RC)^2 \tag{11}$$

It follows that

$$Z_R \Delta = R \tag{12}$$

$$Z_I = Z_R(\omega RC) \Rightarrow \omega RC = \frac{Z_I}{Z_R} \tag{13}$$

Using Eq. 11 and Eq. 13 into Eq. 12 it is obtained

$$R = Z_R\left[1 + \left(\frac{Z_I}{Z_R}\right)^2\right] \tag{14}$$

$$C = \frac{Z_I}{Z_R}\frac{1}{\omega R} = \frac{Z_I}{\omega\left(Z_R^{\ 2} + Z_I^{\ 2}\right)} \tag{15}$$

Since the films are square in shape, the sheet resistance is identical to surface resistance, R. Thus, it follows that the surface conductivity of the graphene film is given by

$$\sigma = \frac{1}{Rt}, \tag{16}$$

where t is the film thickness.

The measured data for the graphene-loaded ring resonator with a film thickness of 10 µm corroborates with the simulated data (see Figure 69) corresponding to a surface impedance of $Z_S = Z_R - jZ_I = 20 - j30$ Ωs per square used in the simulation. It follows from Eq. 14 and Eq. 16 that the RF conductivity of the graphene film is given by 1,540 S/m. The capacitance C determined form Eq. 15 is 0.9 pF at the resonant frequency of 3.97 GHz.

Parametric simulation has been done by varying the resistance (R) and reactance (X) of the surface impedance as shown in Figure 69 and Figure 70.

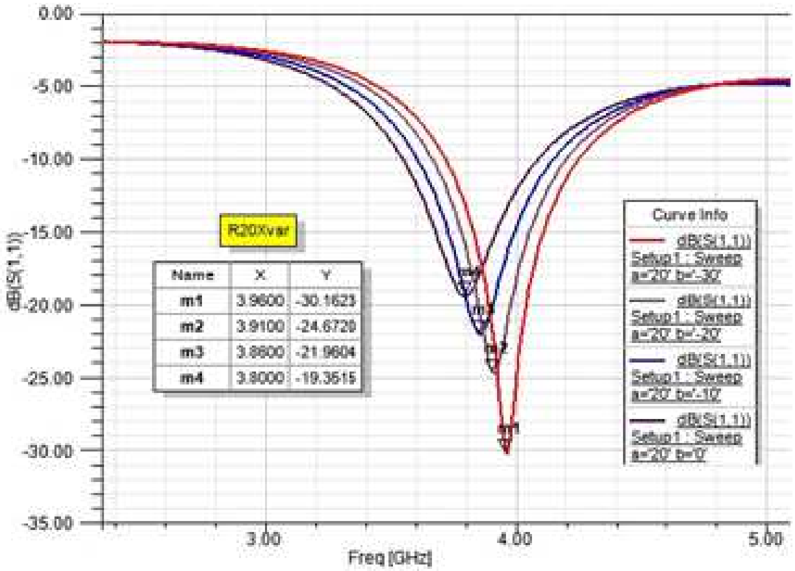

Name	X	Y
m1	3.9600	-30.1623
m2	3.9100	-24.6720
m3	3.8600	-21.9604
m4	3.8000	-19.3515

Figure 65. Parametric simulation: R=a=20 Ω & X=b varies from -30 to 0.

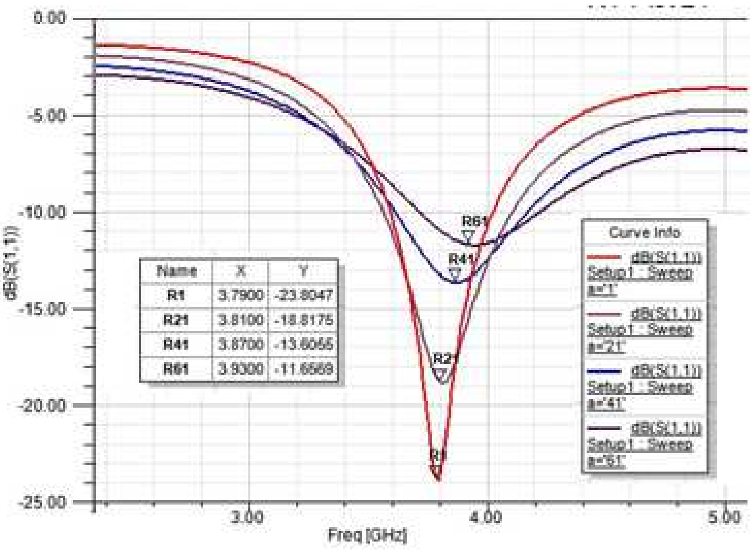

Figure 70. Parametric simulation: X=0 & R=a varies from 1 to 61 Ω.

The results show that by increasing the reactance from -30 to 0 at fixed resistance of 20 Ω, return loss increases from -30 to -19 dB while the frequency decreases from 3.96 to 3.8 GHz. In case of making the reactance fixed at 0 and resistance variation, it is seen that by increasing the resistance from 1 to 61 Ω, return loss increases from -24 to -12 dB as well as the frequency from 3.8 to 3.93 GHz.

6.5 Application as a gas sensor

The ring resonator loaded with graphene film exposed to ammonia gas in order to test its sensibility towards the gas. The photo of the lab is shown in Figure 71.

Sensors were tested in a home-made system where ammonia in helium (450 ppm) was diluted with synthetic air by means of flow meters (Teledyne Hastings Instruments HFM 300 controller and flow meters HFC 302, Teledyne Hastings, Hampton, VA, USA) in a constant air flow of 1000 SCCM (standard cubic centimeters per minute). The investigated range of ammonia concentration was 1 – 50 ppm.

All the sensors were heated by a Ni-Cr wire, located underneath the sensor, alimented with a DC power supply (Peak Tech, Nanjing, Jiangsu, China). A PT1000 resistance temperature detector (RS Pro, London, UK) was used for sensors temperature determination. Two different sensors were then tested between 150°C and 250°C in a chamber having a volume of 0.1 L. The films' impedance was measured by means of a LCR meter (Hioki 3533-01, Nagano, Japan) by alimenting the sensors with an AC tension of 1 V at 1 kHz. Finally, cross sensitivity measurements were carried out towards CH4 (50.0 ppm in air), CO (10.0 ppm in air), N2O (15.0 ppm in air), CO2 (500.0 ppm in air), O3 (0.5 ppm in air), NO2 (0.1 ppm in air), and humidity (50% of relative humidity at room temperature) under the same flow of 1000 SCCM.

Figure 71. Gas sensing experiment

The normal ampoule used for this experiment shown in Figure 72. Regarding that our sensor has 5 cm length and width and does not pass through the ampoule, a plastic box shown in Figure 73 used to satisfy our requirements. It is done by making two holes on the top of the box, one for passing the gas and the other for passing the Network Analyzer cable.

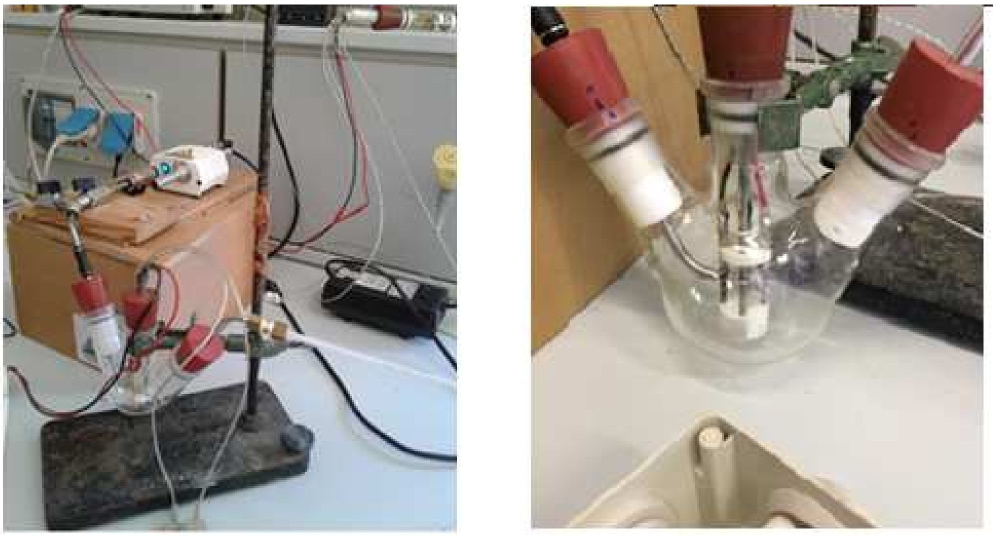

Figure 72. Ampoule

Figure 73. The replaced plastic box

The results shown in Figure 74 highlights that the presence of ammonia gas has some effects on the return loss as well as the resonant frequency which can be sensed and used as a gas sensor. The frequency shift is about 50 MHz from 2.25 GHz for the graphene-loaded ring in air to 2.3 GHz for the graphene-loaded ring in ammonia ambient. The return loss for the former is about -24 dB when for the latter is around -37 dB.

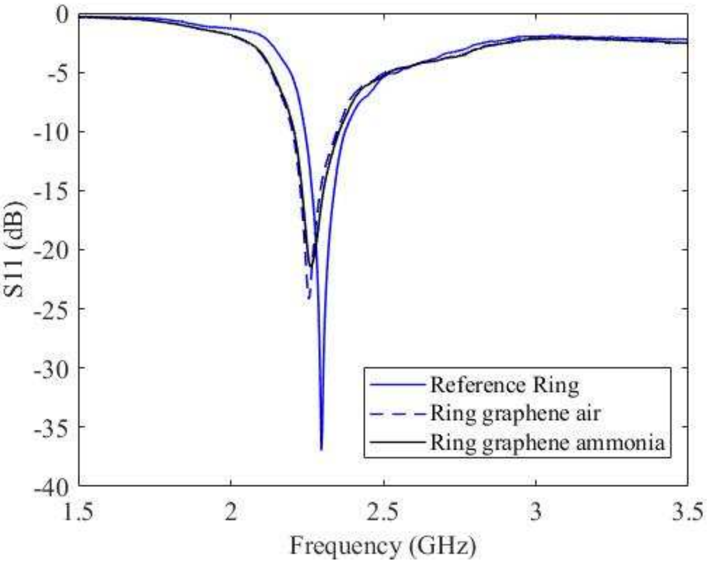

Figure 74. Measurement of graphene-loaded ring resonator in various ambient

Chapter 7

Conclusion

In this thesis, the material parameters and electrical conductivity of graphene films in the microwave region of the electromagnetic spectrum were experimentally investigated. Possible application of composite graphene films at the microwave frequencies shows that it is useful in wireless (RF) sensor applications. Detailed investigation of the surface morphology of the films using SEM, AFM reveals that the graphene filler is was homogeneously dispersed over the film surface with a comparatively lower surface roughness at higher concentrations, and negligible agglomerates. Uniform distribution of the filler into the composite's polymeric matrix can be achieved, at high graphene (i.e. 33% in weight) concentrations, by a proper combination of binders and dispersants (i.e. PVB, PVP, and linoleic acid). Sheet resistance measurement using the four-probe method on bare films compares reasonably well with the surface resistance derived from a full-wave analysis of films printed in between copper electrodes on FR-4 substrate. More specifically, an increasing trend in the conductivity, with the number of printed layer and concentration of graphene was found. Furthermore, dielectric spectroscopy suggested a low-frequency (up to tens of MHz) behavior predicated on an insulating matrix (with storage and dissipative components) percolated by a conductive filler associated to a chemical (quantum) capacitance and to an electron transport resistance.

Moreover, a circuit model of thick films loaded with different amounts of graphene have been presented and discussed. Films made of binder alone, as well as binder plus graphene (weight fraction of 12.5% and 25%), were printed across the gap of microstrip lines, and experimentally studied to produce a circuit model in ADS. The S-parameter results reveal that low (12.5% in weight upon the screen printing paste total mass) graphene loadings have negligible impact on the RF properties of the ethyl cellullose binder used for the polymer thick film deposition. Therefore lightly loaded graphene films are prone to behave like “lossy” insulators where the dielectric loss is dominated by the substrate and binder. On the other hand, S-parameter measurements of graphene films 25% in weight fit with an equivalent circuit comprised of a single RC parallel element. Such a model can be easily ascribed to the formation of nano-capacitors composed of graphene nano-platelets distributed into an insulating matrix (film's binder and FR-4 substrate).

In addition, microstrip, patch antenna and ring resonator structures loaded with the graphene composites were fabricated to investigate the electrical properties of the films in the microwaves. To be added an aperture coupled patch antenna with InterDigitated Capacitor (IDC) loaded with graphene film was simulated to investigate the effect of the film in resonance frequency shift. Transmission (and reflection) coefficients of copper etched microstrip turned out to depend not only on the graphene concentration but also on the binder composition. Different resonance frequency shifts associated to an inductive reactance behavior was found for the various graphene concentrations which can be sensed and used as sensor applications such as gas and bio sensors. In this study, the focus was on gas sensor application.

Future studies are focused on realizing the aperture coupled patch antenna with IDC loaded with graphene film in laboratory. Investigation on using graphene films in periodic structures in microstrip transmission line and measuring its dispersion diagram and transmission coefficient is another future objective.

Further studies to clarify the influence of ethyl cellulose, PVB, PVP different polarity, polarizability), and capability of creating hydrogen bonds on the surface impedance of graphene in the microwaves region are currently taking place. Moreover, the covalent adsorption of “small surfactants” (i.e. linoleic acid) on the graphene surface and its effect on RF electrical properties is also being investigated.

References

[1] S. Novikov, A. Satrapinsky, N. Lebedeva, I. Iisakka, “Fabrication and Study of Large Area QHE Devices Bases on Epitaxial Graphene,” vol. 64, no. 6, pp. 1533-1538, IEEE Transaction on Instrumentation and Measurements, June 2015.

[2] Y.Xu et al. “High-Resolution Patterning of Graphene by Screen Printing with a Silicon Stencil for Highly Flexible Printed Electronics” Adv. Mater. 2015, 27, 109–1115.

[3] S.Tonello, G. Abate, M. Borghetti, M. Marziano, M. Serpelloni, D.L. Uberti, N.F. Lopomo, M. Memo, E. Sardini, “Wireless Point-of-Care Platform With Screen-Printed Sensors for Biomarkers Detection,” IEEE Transaction on Instrumentation and Measurements, 2017.

[4] Z. Zhu, L. G.-Gancedo, A. J. Flewitt, H. Xie, F. Moussy and W. I. Milne, “A Critical Review of Glucose Biosensors Based on Carbon Nanomaterials: Carbon Nanotubes and Graphene,” Sensors, vol. 12, pp. 5996-6022, 2012.

[5] E. W. Hill, A. Vijayaragahvan, and K. Novoselov, “Graphene sensors” IEEE Sensors Journal, vol. 11, no. 12, pp. 3161-3170, Dec. 2011.

[6] W.J. Hyun, E.B. Secor, M.C. Hersam, C.D. Frisbie, L.F. Francis, “High-Resolution Patterning of Graphene by Screen Printing with a Silicon Stencil for Highly Flexible Printed Electronics,” Advanced Materials, vol. 27, no.1, pp.109-1115, 2015.

[7] S. Novikov, A. Satrapinsky, N. Lebedeva, I. Iisakka, “Sensitivity Optimization of Epitaxial graphene-based gas sensors,” vol. 62, no. 6, pp. 1859-1864, IEEE Transaction on Instrumentation and Measurements, June 2013.

[8] H. Lee, G. Shaker, K. Naishadham, X. Song, M. McKinley, B. Wagner, and M. M. Tentzeris, "Carbon nanotube loaded antenna-based ammonia gas sensor," IEEE Trans. Microwave Theory Tech., vol. 59, no. 10, pp. 2665-2673, Oct. 2011.

[9] A.M. Pernia, M.G.Prieto, I.C. Orille, J.A. Martin-Ramos, A. Costa-Garcia, “Development of Optimozed screen-printed immunosensors,” vol. 58, no. 7, pp. 2181-2188, IEEE Transaction on Instrumentation and Measurements, July 2009.

[10] V.K. Nagareddy et al., “Improved Chemical Detection and Ultra-Fast Recovery Using Oxigen Functionalized Epitaxial Graphene Sensors,” vol. 13, no. 8, pp. 2810-2817, IEEE Sensor Journal, August 2013.

[11] M.A. Real et al., “Graphene Epitaxial Growth on SiC (0001) for resistance standards,” vol. 62, no. 6, pp. 1454-1460, IEEE Transaction on Instrumentation and Measurements, June 2013.

[12] Y. Fukuyama et al., “Controlling the Fermi level in a single layer Graphene QHE device for Resistance Standards,” vol. 64, no. 6, pp. 1451-1454, IEEE Transaction on Instrumentation and Measurements, June 2015.

[13] X. Leng, W. Li, D. Luo, F. Wang, “Differenzial Structure with Graphene Oxide for both Humidity and Temperature Sensing,” vol. 17, no. 14, pp. 4357-4364, IEEE Sensor Journal, July 15, 2017.

[14] K. Naishadham, “An investigation on the tunning of a microstrip patch antenna using carbon nanotube thin films,” IEEE Antennas Propagat., Symp., Memphis, USA, July 2014.

[15] K. Naishadham, “Design of a Graphene Loaded Slot Antenna with 100:1 Bandwidth for Wireless Sensor Applications,” IEEE Antennas Propagat., Symp., Memphis, USA, July 2014.

[16] P. Savi, K. Naishadham, A. Bayat, M. Giorcelli, and S. Quaranta, “Multi-Walled Carbon Nanotube Thin Film Loading for Tuning Microstrip Patch Antennas,” Tenth European Conference on Antennas and Propagation (EuCAP), Davos, Switzerland, April 2016.

[17] P. Savi, K. Naishadham, S. Quaranta, M. Giorcelli, A. Bayat, C. Ramella, “Design of a Graphene-Loaded Slotted Ring Resonator for Sensor Applications,” Eleventh European Conference on Antennas and Propagation (EUCAP), Paris, France, March 19-24, pp. 1-4, 2017.

[18] P. Savi, K. Naishadham, S. Quaranta, M. Giorcelli, A. Bayat, “Microwave Characterization of Graphene Films for Sensor Applications,” IEEE International Instrumentation and Measurement Technology Conference (I2MTC), Torino, Italy, May 22-25. pp. 1-5, 2017.

[19] F. Costa, , “Surface Impedance Measurements of Resistive Coatings at Microwave Frequencies,” vol. 62, no. 2, pp. 432-437, IEEE Transaction on Instrumentation and Measurements, Feb. 2013.

[20] S. Chopra, A. Pham, J. Gaillard, A. Parker, and A. M. Rao, “Carbon-nanotube-based resonant-circuit sensor for ammonia,” Appl. Phys. Lett., vol. 80, no. 24, pp. 4632-4634, June 2002.

[21] H. Lee, K. Naishadham, M. M. Tentzeris, and G. Shaker, “A novel highly sensitive antenna-based gas sensor utilizing carbon nanotubes and inkjet printing,” in Proc. IEEE Antennas and Propagation Symposium, Spokane, WA, July 2011.

[22] T. Zhang, S. Mubeen, E. Bekyarova, B. Y. Yoo, R. C. Haddon, N. V.Myung, and M. A.Deshusses, “Poly(m-aminobenzene sulfonic acid) functionalized single-walled carbon nanotube based gas sensor,” Nanotechnology, vol. 18, pp. 165504-165509, 2007.

[23] D. M. Pozar, “A Microstrip Antenna Aperture Coupled to a Microstrip Line”, Electronics Letters, vol. 21, pp. 49-50, January 17, 1985.

[24] D. M. Pozar, “Microstrip antennas”, IEEE Proc., vol. 80, pp. 79-91, January 1992.

[25] D. M. Pozar and D. H. Schaubert, Microstrip Antennas: The Analysis and Design of Microstrip Antennas and Arrays, IEEE Press, New York, 1995.

[26] C.A. Balanis, Antenna Theory, 4nd edition. New York: John Wiley & Sons, Inc., 2016.

[27] Geim, A.K.; Novoselov, K. S. The rise of grapheme. Nat. Mater. 2007, 6, 183–191.

[28] Geim, A.K. Graphene: Status and prospects. Science 2009, 324, 1530-1534.

[29] Li, B.; Zhong W.-H. Review on polymer/graphite nanoplatelet nanocomposites. Mater. Science 2011, 46, 5595-5614.

[30] Cao, X.; Chen, H.; Gu, X.; Liu, B.; Wang, W.; Cao, Y.; Wu, F.; Zhou, C. Screen Printing as a Scalable and Low-Cost Approach for Rigid and Flexible Thin-Film Transistors Using Separated Carbon Nanotubes. ACS Nano 2014, 8, 12769-12776.

[31] Jones, C.S.; Lu, X.; Renn, M.; Stroder, M.; Shih, W.-S. Aerosol-jet-printed, high-speed, flexible thin-film transistor made using single-walled carbon nanotube solution. Microelectron. Eng. 2010, 87, 434-437.

[32] Zhou, Y.; Hu, L.; Grüner, G. A method of printing carbon nanotube thin films. Appl. Phys. Lett. 2006, 88, 109-123.

[33] Liu, C.-X.; Choi, J.-W. Patterning conductive PDMS nanocomposite in an elastomer using microcontact printing. J. Micromech. Microeng. 2009, 19, 085019.

[34] Kymakis, E.; Stratakis, E.; Stylianakis, M.M.; Koudoumas, E.; Fotakis, C. Spin coated graphene films as the transparent electrode in organic photovoltaic devices. Thin Solid Films 2011, 520, 1238-1241.

[35] Bedzyk, M.J.; Arnold, M.S.; Hersam, M.C.; Guisinger, N.P. Electronic and mechanical properties of Graphene-Germanium interfaces grown by Chemical Vapor Deposition. Nano Lett. 2015, 15, 7414−7420.

[36] Su, W.; Xu, J.; Ding, X. An Electrochemical pH Sensor Based on the Amino-Functionalized Graphene and Polyaniline Composite Film. IEEE Trans. on Nanobioscience 2016, 15, 812-819.

[37] Chou, J.-C.; Chen, J.-S.; Liao, Yi-H.; Lai, C.-H.; Yan, S.-J.; Huang, M.-S.; Wu, T.-Y. Fabrication and Characteristic Analysis for Enzymatic Glucose Biosensor Modified by Graphene Oxide and Magnetic Beads Based on Microfluidic Framework. IEEE Sensors Journal 2017, 17, 1741-1748.

[38] Sanaeepour, M.; Abedi, A.; Sharifi, M.J. Performance Analysis of Nanoscale Single Layer Graphene Pressure Sensors. IEEE Trans. on Electron Devices 2017, 64, 1292-1296.

[39] Zinenko, T.L.; Matsushima, A.; Nosich, A.I. Surface-plasmon, grating-mode and slab-mode resonances in THz wave scattering by a graphene strip grating embedded into a dielectric slab. IEEE J. Sel. Topics Quant. Electron. 2017, 23, Art. No. 4601809.

[40] Dragoman, M.; Neculoiu, D.; Dragoman, D.; Deligeorgis, G.; Konstantinidis, G.; Cismaru, A.; Coccetti, F.; Plana, R. Graphene for Microwave. IEEE Microwave Magazine 2010, 11, 81-86.

[41] Bozzi, M.; Pierantoni, L.; Bellucci, S. Applications of Graphene at Microwave Frequencies. Radioengineering 2015, 24, 661-669.

[42] Pierantoni, L.; Mencarelli, D.; Bozzi, M.; Moro, R.; Moscato, S.; Perregrini, L.; Micciulla, F.; Cataldo, A.; Bellucci, S. Broadband Microwave Attenuator Based on Few Layer Graphene Flakes. IEEE Transactions on Microwave Theory and Techniques 2015, 63, 2491-2497.

[43] Nilavalan, R.; Craddock, I.J.; Preece, A.; Leendertz, J.; Benjamin, R. Wideband microstrip patch antenna design for breast cancer tumour detection. IET Microw. Antennas Propag. 2007, 1, 277–281.

[44] Yasir, M.; Savi, P.; Bistarelli, S.; Cataldo, A.; Bozzi, M.; Pellegrini, L.; Bellucci, S. A Planar Antenna with Voltage-Controlled Frequency Tuning Based on Few-Layer Graphene. IEEE Antennas and Wireless Propagation Letters 2017, 16, 2380-2383.

[45] Bokobza, L.; Bruneel, J.-L.; Couzi, M. Raman Spectra of Carbon-Based Materials (from Graphite to Carbon Black) and of Some Silicone Composites. Graphene Nanocomp. for Adv. App. 2015, 1, 77-94; DOI:10.3390/c1010077.

[46] Peter J. F. Harris, Transmission Electron Microscopy of Carbon: A Brief History, C 2018, 4, 4; doi:10.3390/c4010004

[47] H. Dai, “Carbon Nanotubes:Synthesis, Integration and Properties,” Accounts of Chemical Research, vol. 35, no.12, pp.1035-1044, 2002.

[48] T.E.Chang, A. Kisliuk, S.M. Rhodes, W.J. Brittain, A.P. Sokolov, Conductivity and mechanical properties of well-dispersed single-wall carbon nanotube/polystyrene composites," Polymer, vol. 47, pp.7740-7746, 2006.

[49] H. Mosallaei and K. Sarabandi, "Magneto-dielectrics in electromagnetics: concept and applications," IEEE Trans. Antennas Propagat., vol. 52, no. 6, pp. 1558-1567, June 2004.

[50] G.-M Yang, K. Naishadham and N. X. Sun, "Loading effects of self-biased magnetic films on patch antennas with substrate/superstrate sandwich structure," IET Microwaves, Antennas Propagat., vol. 4, no. 9, pp. 1172-1181, Sep. 2010.

[51] J.H. Park, P.S. Alegaonkar, S.Y. Jeon, J.B. Yoo, "Carbon nanotube composite: Dispersion routes and field emission parameters," Composites Science and Technology 68, pp. 753–759, 2008.

[52] J. Xia, F. Chen, J. Li, and N. Tao. Graphene Terahertz plasmon oscillators, IEEE Trans. Nanotechnol., 2008, 7, 91–99.